cytoplasm or the nucleus (Supplemental Figure 4A). The increase in Hes1 or Hey1 was not detected by immunostaining analysis at this period (Supplemental Figure 4B and Supplemental Figure 5B), but the abundance of mRNAs for *Hes1*, *Hey1*, and *Hey2* was increased in the livers of *Mx1*-Cre/*Fbxw7*$^{F/F}$ mice at 50 weeks after pIpC injection (Figure 6D). Neither Notch2, mutations in the gene in which mutations result in Alagille disease, nor Notch3 or Notch4, the expression of both of which is increased in hepatocellular carcinoma, were detected by immunofluorescence analysis in the livers of either control or *Mx1*-Cre/*Fbxw7*$^{F/F}$ mice (data not shown). However, neither the expression of Notch ligands, such as Dll-1 and Jagged-1, nor that of the Notch cofactor RBP-J in the liver appeared to be affected by the loss of Fbxw7 (Supplemental Figure 6). We also examined the expression of TSC1 and TSC2, given that the loss of function of either TSC1 or TSC2 is known to result in the development of hamartoma in humans. However, no difference in expression of TSC1 or TSC2 was found between Fbxw7-deficient and control mice (Supplemental Figure 6).

To investigate whether the skewed developmental orientation toward the cholangiocyte lineage apparent in the Fbxw7-deficient liver is dependent on Notch1 accumulation, we examined the differentiation of hepatic stem cells in culture (45). A fraction containing hepatic stem cells was prepared from the livers of *Fbxw7*$^{+/F}$ and *Fbxw7*$^{F/F}$ embryos and was then infected with a retrovirus encoding Cre recombinase or with the empty virus alone to generate *Fbxw7*$^{+/F}$, *Fbxw7*$^{+/\Delta}$, *Fbxw7*$^{F/F}$, and *Fbxw7*$^{\Delta/\Delta}$ cells in the presence of HGF and EGF. Immunofluorescence analysis revealed that most of the *Fbxw7*$^{+/F}$, *Fbxw7*$^{+/\Delta}$, and *Fbxw7*$^{F/F}$ cells differentiated into the hepatocyte lineage, characterized by albumin expression, with only a small subset of cells differentiating into the cholangiocyte lineage (Figure 7A). In contrast, the percentage of *Fbxw7*$^{\Delta/\Delta}$ cells that differentiated into the cholangiocyte lineage, characterized by expression of CK7, was markedly increased compared with that for cells of the control genotypes. To confirm these results in a quantitative manner, we performed RT and real-time PCR analysis of *Alb* and *CK19* mRNAs. Consistent with the immunofluorescence data, the amount of *CK19* mRNA was significantly increased in *Fbxw7*$^{\Delta/\Delta}$ cells compared with that in *Fbxw7*$^{+/\Delta}$ cells, whereas the abundance of *Alb* mRNA did not differ between the 2 genotypes (Figure 7B).

Notch signaling is implicated in the differentiation of liver stem cells into the cholangiocyte lineage. Indeed, immunofluorescence analysis revealed that Notch1 accumulated in *Fbxw7*$^{\Delta/\Delta}$ cells to a greater extent than in *Fbxw7*$^{+/\Delta}$ cells (Supplemental Figure 7). We therefore examined whether additional ablation of the Notch cofactor RBP-J might correct the abnormal development of Fbxw7-deficient liver stem cells. We generated Fbxw7-deficient hepatic stem cells with additional deletion of either *Rbpj* or *Myc* genes and examined the level of *CK19* mRNA. The abundance of *CK19* mRNA was increased in *Fbxw7*$^{\Delta/\Delta}$*Myc*$^{\Delta/\Delta}$ cells but not in *Fbxw7*$^{\Delta/\Delta}$*Rbpj*$^{\Delta/\Delta}$ cells (Figure 7B). These results indicate that the skewed developmental orientation of hepatic stem cells to the cholangiocyte lineage is dependent on Notch1 accumulation induced by the loss of Fbxw7.

Discussion

Given that the substrates of Fbxw7 include key proteins that contribute to diverse biological processes, including the cell cycle, cell differentiation, and apoptosis, and that the binding of Fbxw7 to its substrates depends on their phosphorylation, the function of this protein is likely complex. Although much attention has focused on the relation between the accumulation of cyclin E due to loss of Fbxw7 function and tumorigenesis, Notch degradation by Fbxw7 is critical during embryogenesis, suggesting that Fbxw7 functions in development- and tissue-dependent manners. To provide insight into the physiological and pathological relevance of Fbxw7, we have induced conditional inactivation of *Fbxw7* in several mouse tissues. Our previous studies have shown that ablation of *Fbxw7* in hematopoietic cells or fibroblasts results in abnormalities that are mainly related to the cell cycle and apoptosis. We now show that liver-specific ablation of *Fbxw7* induced fatty liver and abnormal cell differentiation, likely as a result of the accumulation of SREBPs and Notch1, respectively, as well as promoted cell proliferation (Figure 8).

We generated 2 types of mice with liver-specific deficiency of Fbxw7 with the use of the *Mx1* or *Alb* gene promoters to drive Cre expression. The phenotypes of *Alb*-Cre/*Fbxw7*$^{F/F}$ mice are milder than those induced by acute ablation of Fbxw7 in *Mx1*-Cre/*Fbxw7*$^{F/F}$ mice, probably because of the operation of compensatory mechanisms during development in the former animals. In *Mx1*-Cre/*Fbxw7*$^{F/F}$ mice, it would be expected for *Fbxw7* to be deleted in cells and tissues other than the liver, such as hematopoietic cells. To exclude the possibility that ablation of Fbxw7 in hematopoietic cell lineages might be responsible for steatohepatitis, we have generated Lck-Cre/*Fbxw7*$^{F/F}$ and CD4-Cre/*Fbxw7*$^{F/F}$ mice (in both of which *Fbxw7* deletion occurs in T cells), CD19-Cre/*Fbxw7*$^{F/F}$ mice (*Fbxw7* deletion occurs in B cells), and LysM-Cre/*Fbxw7*$^{F/F}$ mice (*Fbxw7* deletion occurs in myeloid cells). None of these animals showed either fatty liver or hepatic inflammation (data not shown). Furthermore, *Alb*-Cre/*Fbxw7*$^{F/F}$ mice manifested pronounced hepatic infiltration of inflammatory cells when they were fed an MCD diet, confirming that the steatohepatitis induced by *Fbxw7* deletion is attributable to an effect that is intrinsic to the liver.

Nonalcoholic fatty liver disease (NAFLD) is a growing health concern, due to its rapidly increasing prevalence worldwide. NASH is a progressive form of NAFLD that has the potential to develop into hepatocellular carcinoma. We now show that mice with liver-specific ablation of Fbxw7 developed clinicopathologic features similar to those of NAFLD or NASH in humans, including triglyceride deposition around central veins, pericellular fibrosis, infiltration of inflammatory mononuclear cells, and the appearance of Mallory bodies in the liver as well as increases in the serum levels of ALT and AST. However, these animals were not found to develop hepatocellular carcinoma. Genetic mouse models for human NASH have been established by functional deletion of leptin (46) or its receptor (47), phosphatase and tensin homolog (PTEN) (48), NEMO (also known as IKK-γ) (49), interleukin-1 receptor α (50), galectin-3 (51), or retinoic acid receptor α (52). Mice transgenic for SREBP1c also manifest pronounced NASH (53). SREBP1c is degraded in an Fbxw7-dependent manner (16), and we have now shown that it accumulated in the Fbxw7-deficient liver. These findings thus suggest that an Fbxw7-SREBP1 axis plays a key physiological role in the regulation of lipid metabolism in the liver as well as a pathological role in the development of NASH.

Whereas steatosis develops in the acute phase of liver-specific Fbxw7 deficiency, hamartoma develops in the chronic phase. Fbxw7 targets mTOR for degradation (19). The TSC complex, consisting of TSC1 (hamartin) and TSC2 (tuberin), is the major negative regulator of mTOR, and its genetic loss results in mTOR

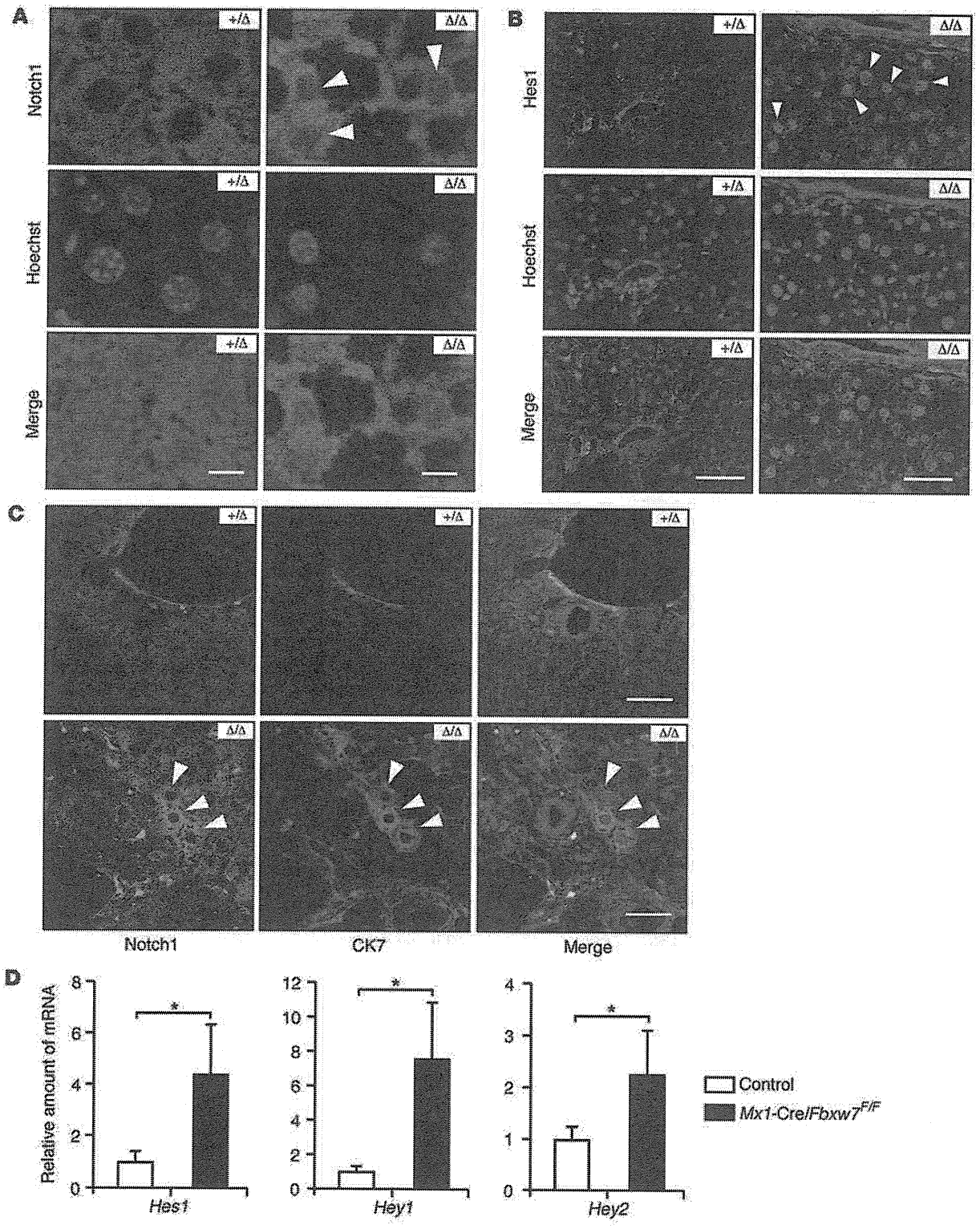

Figure 6

Accumulation of Notch1 and activation of its target genes in the Fbxw7-deficient liver. (**A** and **B**) Representative immunostaining for the intracellular domain of (**A**) Notch1 and for (**B**) Hes1 in liver sections from *Mx1*-Cre/*Fbxw7*$^{+/F}$ (+/Δ) and *Mx1*-Cre/*Fbxw7*$^{F/F}$ (Δ/Δ) mice at 3 weeks after *Fbxw7* deletion by pIpC injection, beginning at 8 weeks of age. Arrowheads indicate accumulating (**A**) Notch1 intracellular domain and (**B**) Hes1 in the nucleus. (**C**) Immunofluorescence staining for the intracellular domain of Notch1 and for CK7 in the livers of *Mx1*-Cre/*Fbxw7*$^{+/F}$ (+/Δ) and *Mx1*-Cre/*Fbxw7*$^{F/F}$ (Δ/Δ) mice at 15 weeks after the final injection of pIpC, beginning at 8 weeks of age. Intense Notch1 staining was detected in the Fbxw7-deficient liver, and most of the Notch1-positive cells express CK7 (arrowheads). Scale bar: 10 μm (**A**); 50 μm (**B** and **C**). (**D**) RT and real-time PCR analysis of Notch target genes in the livers of *Mx1*-Cre/*Fbxw7*$^{+/F}$ (control) and *Mx1*-Cre/*Fbxw7*$^{F/F}$ mice at 50 weeks after *Fbxw7* deletion. Normalized data for *Hes1*, *Hey1*, and *Hey2* mRNAs are expressed relative to the corresponding value for control mice and are mean ± SD from 3 independent experiments. $^{*}P < 0.05$.

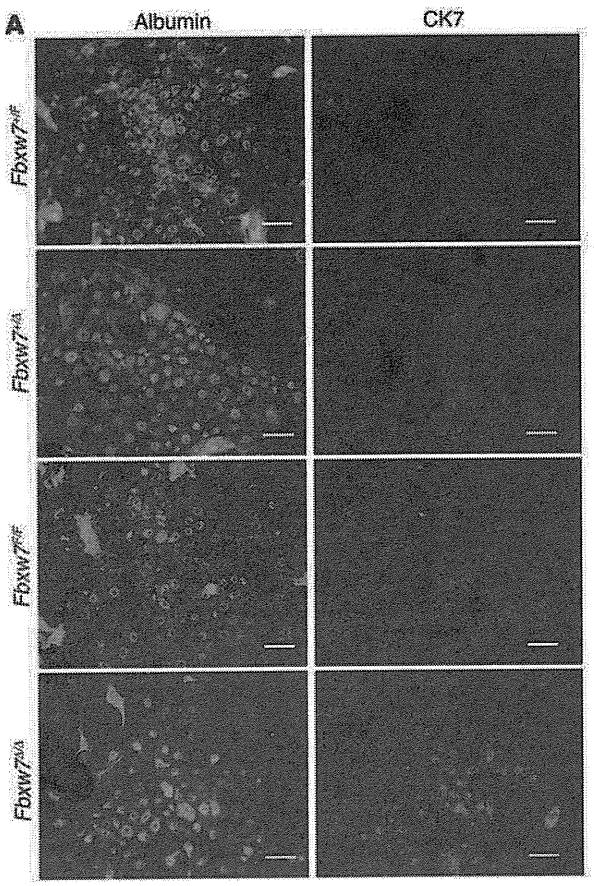

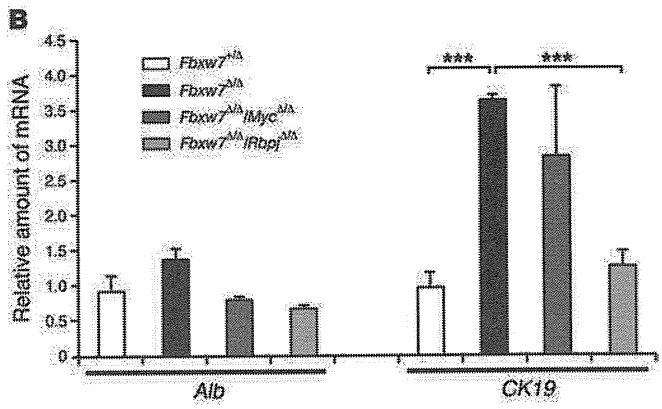

Figure 7
Skewed differentiation of hepatic stem cells from Fbxw7-deficient mice. (**A**) Primary cultured liver cells of the indicated genotypes were subjected to immunofluorescence staining with antibodies to albumin or to CK7. Clusters of cells expressing CK7 were apparent only with *Fbxw7*$^{\Delta/\Delta}$ cells. Scale bar: 50 μm. (**B**) RT and real-time PCR analysis of *Alb* and *CK19* mRNAs in primary cultured liver cells of the indicated genotypes. Normalized data for *Alb* and *CK19* mRNAs are expressed relative to the corresponding value for *Fbxw7*$^{+/\Delta}$ cells. Data are mean ± SD from 3 independent experiments. ***$P < 0.005$.

activation and development of hamartoma in humans (54, 55). However, the abundance of mTOR or TSC1/2 was not altered in the Fbxw7-deficient livers of mice, suggesting that the accumulation of mTOR or the loss of TSC1/2 is not responsible for hamartoma development in these animals. Microscopic examination revealed over proliferation of the biliary system in the hamartomas, suggesting that deregulated differentiation of liver stem cells into the cholangiocyte lineage might be largely responsible for hamartoma development. Liver stem cells are able to differentiate into either the hepatocyte or cholangiocyte lineages, with the Notch signaling pathway having been implicated in regulation of the cell fate decision by skewing differentiation toward the cholangiocyte lineage (41). We have now shown that both Notch1 and its target genes were overexpressed in the Fbxw7-deficient livers of mice and that the abnormal cell differentiation induced by Fbxw7 loss was corrected by the additional loss of the Notch cofactor RBP-J. These results suggest that Notch1 accumulation as a result of Fbxw7 loss is primarily responsible for the abnormal cell differentiation in the Fbxw7-deficient mouse liver. Although the origin of hamartomas as well as the mechanism of their development in the Fbxw7-deficient liver are currently unclear, transient activation of Notch proteins as a result of Fbxw7 loss may lead to a shift in cell differentiation from hepatocytes to cholangiocytes, and the generation of such abnormally differentiated cells might confer a predisposition to hamartoma development that is realized if the cells undergo an additional gene mutation. Mice lacking both Foxa1 and Foxa2 were recently shown to display a similar liver phenotype (hyperplasia of the biliary tree) (56). However, neither differentiation of hepatocytes nor Notch signaling were affected in Foxa1/2-deficient mice, whereas hyperactivation of Notch signaling seems to be attributable to the bile duct hamartoma in Fbxw7-deficient mice. Furthermore, proliferation of relatively small and uniform bile ducts is prominent in Foxa1/2-deficient mice, whereas the abnormal bile ducts in Fbxw7-deficient mice are large and heterogeneous in size. We therefore concluded that the mechanism underlying the development of proliferative bile ducts is likely different between these mutant mice.

Although Fbxw7 had been thought to function primarily in cell cycle control by regulating cyclin E, c-Myc, Notch, and c-Jun, the recent identification of additional substrates has suggested new cell cycle–independent roles for Fbxw7. We now provide genetic evidence that the major substrates of Fbxw7 in the liver are SREBP1 and Notch1, which accumulate in the Fbxw7-deficient liver and are responsible for liver steatosis and hamartoma development, respectively. These results contrast with our previous observations that deletion of *Fbxw7* in the hematopoietic system and fibroblasts results primarily in deregulation of the cell cycle or of apoptosis due to activation of the p53-dependent checkpoint (34–36). Why does the function of Fbxw7 differ in different tissues? We propose that the biological relevance of Fbxw7 is determined by 3 factors: (a) the expression of Fbxw7; (b) the expression and activation of protein kinases that phosphorylate the Cdc4 phosphodegron, an amino acid sequence that is recognized by Fbxw7; and (c) the expression of substrate molecules. The combination of these 3 factors may define the role of Fbxw7 in a tissue-specific manner, with the different phenotypes associated with Fbxw7 deficiency

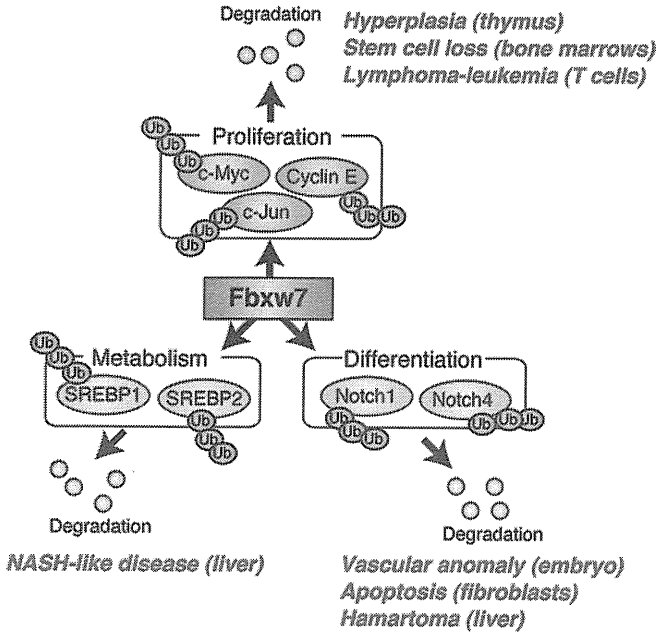

Figure 8
A model for Fbxw7 functions in vivo. Fbxw7 mediates ubiquitin-dependent degradation of substrates in different functional categories. For example, Fbxw7 controls cell proliferation by targeting c-Myc, cyclin E, and c-Jun for degradation. However, it also regulates lipid metabolism and cell differentiation by targeting SREBP and Notch proteins, respectively. Major phenotypes associated with Fbxw7 deficiency in different tissues are shown in red. Ub, ubiquitin.

being attributable to different expression patterns of Fbxw7, its substrates, and kinases that phosphorylate each substrate.

Methods

Generation of conditional knockout mice. Mice homozygous for the floxed *Fbxw7* allele (*Fbxw7*$^{F/F}$ mice) (34) were crossed with *Mx1*-Cre transgenic mice (57) provided by K. Rajewsky (Harvard Medical School, Boston, Massachusetts, USA) or *Alb*-Cre transgenic mice (58) purchased from The Jackson Laboratory. Expression of Cre recombinase in the resulting offspring of the former cross was induced by i.p. injection of 500 μg pIpC (GE Healthcare Biosciences) on 3 alternate days. Deletion of exon 5 of the floxed *Fbxw7* allele was confirmed by PCR analysis of genomic DNA as previously described (34). *Fbxw7*$^{F/F}$ mice were also crossed with *Rbpj*$^{F/F}$ mice (59) provided by T. Honjo (Kyoto University, Kyoto, Japan) or *Myc*$^{F/F}$ mice (60) provided by I.M. de Alborán (National Center for Biotechnology, Madrid, Spain). The experimental protocols were approved by the Institutional Animal Care and Use Committee of Kyushu University.

Histological and biochemical analysis. Liver tissue was fixed with 4% paraformaldehyde in PBS, embedded in paraffin, and stained with H&E or Masson's trichrome solution. Some sections were stained with Oil red O (Nakalai Tesque) according to standard procedures, in order to examine the extent of lipid accumulation in hepatocytes. Serum levels of AST and ALT were measured with a standard clinical autoanalyzer.

Dietary model of NASH. Mice were fed with an MCD diet (Funabashi Farm) for the indicated periods (see the legend for Figure 2) and analyzed.

Measurement of triglyceride and total cholesterol levels in the liver. Frozen liver tissue was homogenized, and triglyceride and total cholesterol were extracted from the homogenate with chloroform/methanol (2:1, vol/vol), dried, and resuspended in 2-propanol. The amounts of triglyceride and total cholesterol in the extract were measured with the use of Lipidos liquid and Cholescolor liquid kits (Toyobo), respectively.

Immunoblot analysis. Total protein extracts were prepared from liver with RIPA buffer. The extracts (30 μg) were subjected to immunoblot analysis as described previously (61) with antibodies to cyclin E (M-20), to c-Myc (N-262), to ChREBP (P-13), or to PPAR-γ (E-8), all of which were obtained from Santa Cruz Biotechnology Inc.; with antibodies to Ser^{2448}-phosphorylated or total (7C10) forms of mTOR (Cell Signaling Technology); with antibodies to SREBP1 (2A4, NeoMarkers); or with antibodies to PGC-1α (Chemicon). As a control, each membrane was stripped and then probed with antibodies to Hsp90 (BD Transduction Laboratories).

RT and real-time PCR analysis. Total RNA was extracted from liver using the guanidinium thiocyanate–phenol-chloroform method, purified, and subjected (1 μg) to RT with random hexanucleotide primers (ReverTra Ace α, Toyobo). The resulting cDNA was subjected to real-time PCR in a reaction mixture that contained 1× SYBR Green PCR Master Mix (Applied Biosystems) and 200 nM of gene-specific primers. Assays were performed in triplicate with an ABI Prism 7700 Sequence Detector (Applied Biosystems). The PCR protocol comprised 40 cycles of incubation at 60°C for 30 seconds and 95°C for 5 seconds. The sequences of the PCR primers (sense and antisense, respectively) were 5′-TGCTCCCAGCTGCAGGC-3′ and 5′-GCCCGGTAGCTCTGGGTGTA-3′ for *Fas*, 5′-TGGGTTGGCTGCTTGTG-3′ and 5′-GCGTGGGCAGGATGAAG-3′ for *Scd1*, 5′-CTGCCGACCTGATGAATTCC-3′ and 5′-TAGGGCCATCACACTGTGTC-3′ for *Ldlr*, 5′-GCTCTCCATACAGTGCTACC-3′ and 5′-GAGTGAAAGATCATGAAGCC-3′ for *Hmgcs1*, 5′-AGAGATGCCATCTCCAGCCTC-3′ and 5′-CTTGGTCTTAGGGTCTTCAGG-3′ for *ChREBP*, 5′-CTGTGAAGTTCAATGCACTGGAA-3′ and 5′-CCTCGATGGGCTTCACGTT-3′ for *Pparg*, 5′-CATGGATTGCACATTTGAAG-3′ and 5′-CCTGTGTCCCCTGTCTCA-3′ for *SREBP1c*, 5′-TCCTGTGCTGCAGCCTTTCTCA-3′ and 5′-CCAGGTTCCCACAAAGGCATCA-3′ for fatty acid–binding protein 4, 5′-GTCCTACAGATTGACAATGC-3′ and 5′-CACGCTCTGGATCTGTGACAG-3′ for *CK19*, 5′-CATGACACCATGCCTGCTGAT-3′ and 5′-CTCTGATCTTCAGGAAGTGTAC-3′ for *Alb*, 5′-CATTCCAAGCTAGAGAAGGCAG-3′ and 5′-TATTTCCCCAACACGCTCG-3′ for *Hes1*, 5′-AAAATGCTGCACACTGCAGG-3′ and 5′-CGAGTCCTTCAATGATGCTCAG-3′ for *Hey1*, 5′-AAACGACCTCCGAAAGCGA-3′ and 5′-CGGTGAATTGGACCTCATCACT-3′ for *Hey2*, and 5′-GGAACATAGCCGTAAACTGC-3′ and 5′-TCACTGTGCCTGAACTTACC-3′ for β-tubulin. Reactions for β-tubulin mRNA were performed concurrently on the same plate as those for the test mRNAs, and results were normalized by the corresponding amount of β-tubulin mRNA.

BrdU incorporation in vivo. Mice were injected with BrdU (1 mg, i.p.) on 3 consecutive days. The liver was removed 24 hours after the third injection of BrdU, and BrdU incorporation was examined with an In Situ BrdU Detection Kit (BD Biosciences). BrdU-positive cells were counted in 10 different fields at high (×400) magnification, and the percentage of BrdU-positive cells was calculated.

Immunofluorescence microscopy. Liver tissue was fixed with 4% paraformaldehyde in PBS and sectioned at a thickness of 40 μm with a vibratome. Sections were then immunostained with antibodies to the intracellular domain of Notch1 or to SCD-1 (both from Cell Signaling Technology), to Hes1 (AB5702, Millipore), to SREBP1 (2A4, NeoMarkers), to albumin (Biogenesis), to CK19 (45), or to CK7 (MAB3226, Chemicon). Immune complexes were detected with Alexa Fluor 488– or Alexa Fluor 546–conjugated goat antibodies to mouse or rabbit IgG (Invitrogen). Cultured liver cells were also subjected to immunostaining, as described previously (45), with the antibodies to albumin and to CK7. For confocal microscopic analysis, we used Zeiss LSM 510 META Confocal Microscope (Carl Zeiss MicroImaging).

TUNEL assay. The TUNEL assay was performed as described previously (62). In brief, paraffin-embedded sections of liver were treated with H_2O_2,

permeabilized for 15 minutes at 37°C with proteinase K (20 μg/ml, Sigma-Aldrich), and then incubated for 1 hour at 37°C with a reaction mixture containing terminal deoxynucleotidyl transferase (Invitrogen) and biotinylated dUTP (Boehringer Ingelheim). Labeled DNA was visualized with an ABC Kit (Vector Laboratories) and diaminobenzidine.

Primary culture of fetal hepatocytes. For the preparation of a single-cell suspension, the livers of mice at E13.5 were dissociated in culture medium (DMEM supplemented with 10% FBS, γ-insulin [1 μg/ml, Wako], 0.1 μM dexamethasone [Sigma-Aldrich], 10 mM nicotinamide [Sigma-Aldrich], 2 mM L-glutamine [Gibco BRL], 50 μM β-mercaptoethanol [Sigma-Aldrich], 5 mM HEPES [Wako], and penicillin-streptomycin [Gibco BRL]) by repeated passage of the tissue through the mouth of a pipette. Human recombinant HGF (50 ng/ml, Sigma-Aldrich) and EGF (20 ng/ml, Sigma-Aldrich) were added to the cells at 24 hours after culture initiation. Cells were seeded at a density of 1×10^6 cells per well in 6-well plates for infection with retroviruses as described below (45).

Gene deletion in cultured cells by retroviral infection. cDNA encoding Cre recombinase was subcloned into the retroviral vector pMX-puro provided by T. Kitamura (University of Tokyo, Tokyo, Japan), and the resulting construct was introduced into Plat E packaging cells (63) with the use of the FuGENE6 reagent (Roche). The resulting culture supernatants containing the recombinant ecotropic retrovirus were harvested and incubated for 24 hours in the presence of Polybrene (2 μg/ml; Sigma-Aldrich) with proliferating liver cells harboring floxed alleles of *Fbxw7*, *Rbpj*, or *Myc*. The cells were cultured for an additional 24 hours in virus-free medium, subjected to selection in medium containing puromycin (3 μg/ml), cultured for 96 hours in puromycin-free medium, and then harvested.

Statistics. Data are presented as mean ± SD and were analyzed using 2-tailed Student's *t* test. A *P* value of less than 0.05 was considered statistically significant.

Acknowledgments

We thank T. Honjo for *Rbpj* floxed mice; I.M. de Alborán for *Myc* floxed mice; K. Rajewsky for *Mx1*-Cre transgenic mice; T. Kitamura for pMX-puro; S. Aishima, Y. Nishihara, M. Sakamoto, and R. Irie for discussion; N. Kitajima, Y. Yamada, and K. Takeda for technical assistance; members of our laboratories for comments on the manuscript; and A. Ohta and M. Kimura for help in the preparation of the manuscript. This work was supported in part by a grant from the Ministry of Education, Culture, Sports, Science, and Technology of Japan and by a research grant from the Takeda Science Foundation.

Received for publication August 6, 2009, and accepted in revised form September 29, 2010.

Address correspondence to: Keiichi I. Nakayama, Department of Molecular and Cellular Biology, Medical Institute of Bioregulation, Kyushu University, 3-1-1 Maidashi, Higashi-ku, Fukuoka, Fukuoka 812-8582, Japan. Phone: 81.92.642.6815; Fax: 81.92.642.6819; E-mail: nakayak1@bioreg.kyushu-u.ac.jp.

1. Hershko A, Ciechanover A. The ubiquitin system. *Annu Rev Biochem.* 1998;67:425–479.
2. Nakayama KI, Nakayama K. Ubiquitin ligases: cell-cycle control and cancer. *Nat Rev Cancer.* 2006; 6(5):369–381.
3. Frescas D, Pagano M. Deregulated proteolysis by the F-box proteins SKP2 and beta-TrCP: tipping the scales of cancer. *Nat Rev Cancer.* 2008;8(6):438–449.
4. Welcker M, Clurman BE. FBW7 ubiquitin ligase: a tumour suppressor at the crossroads of cell division, groWTh and differentiation. *Nat Rev Cancer.* 2008;8(2):83–93.
5. Hubbard EJ, Wu G, Kitajewski J, Greenwald I. *sel-10*, a negative regulator of *lin-12* activity in *Caenorhabditis elegans*, encodes a member of the CDC4 family of proteins. *Genes Dev.* 1997;11(23):3182–3193.
6. Sundaram M, Greenwald I. Suppressors of a *lin-12* hypomorph define genes that interact with both *lin-12* and *glp-1* in *Caenorhabditis elegans*. *Genetics.* 1993;135(3):765–783.
7. Gupta-Rossi N, et al. Functional interaction between SEL-10, an F-box protein, and the nuclear form of activated Notch1 receptor. *J Biol Chem.* 2001;276(37):34371–34378.
8. Oberg C, Li J, Pauley A, Wolf E, Gurney M, Lendahl U. The Notch intracellular domain is ubiquitinated and negatively regulated by the mammalian Sel-10 homolog. *J Biol Chem.* 2001;276(38):35847–35853.
9. Koepp DM, et al. Phosphorylation-dependent ubiquitination of cyclin E by the SCF^{Fbw7} ubiquitin ligase. *Science.* 2001;294(5540):173–177.
10. Moberg KH, Bell DW, Wahrer DC, Haber DA, Hariharan IK. Archipelago regulates Cyclin E levels in Drosophila and is mutated in human cancer cell lines. *Nature.* 2001;413(6853):311–316.
11. Strohmaier H, Spruck CH, Kaiser P, Won KA, Sangfelt O, Reed SI. Human F-box protein hCdc4 targets cyclin E for proteolysis and is mutated in a breast cancer cell line. *Nature.* 2001;413(6853):316–322.
12. Yada M, et al. Phosphorylation-dependent degradation of c-Myc is mediated by the F-box protein Fbw7. *EMBO J.* 2004;23(10):2116–2125.
13. Welcker M, et al. The Fbw7 tumor suppressor regulates glycogen synthase kinase 3 phosphorylation-dependent c-Myc protein degradation. *Proc Natl Acad Sci U S A.* 2004;101(24):9085–9090.
14. Nateri AS, Riera-Sans L, Da Costa C, Behrens A. The ubiquitin ligase SCF^{Fbw7} antagonizes apoptotic JNK signaling. *Science.* 2004;303(5662):1374–1378.
15. Wei W, Jin J, Schlisio S, Harper JW, Kaelin WG Jr. The v-Jun point mutation allows c-Jun to escape GSK3-dependent recognition and destruction by the Fbw7 ubiquitin ligase. *Cancer Cell.* 2005;8(1):25–33.
16. Sundqvist A, et al. Control of lipid metabolism by phosphorylation-dependent degradation of the SREBP family of transcription factors by SCF^{Fbw7}. *Cell Metab.* 2005;1(6):379–391.
17. Punga T, Bengoechea-Alonso MT, Ericsson J. Phosphorylation and ubiquitination of the transcription factor sterol regulatory element-binding protein-1 in response to DNA binding. *J Biol Chem.* 2006;281(35):25278–25286.
18. Bengoechea-Alonso MT, Ericsson J. A phosphorylation cascade controls the degradation of active SREBP1. *J Biol Chem.* 2009;284(9):5885–5895.
19. Mao JH, et al. FBXW7 targets mTOR for degradation and cooperates with PTEN in tumor suppression. *Science.* 2008;321(5895):1499–1502.
20. Olson BL, et al. SCF^{Cdc4} acts antagonistically to the PGC-1alpha transcriptional coactivator by targeting it for ubiquitin-mediated proteolysis. *Genes Dev.* 2008;22(2):252–264.
21. Maser RS, et al. Chromosomally unstable mouse tumours have genomic alterations similar to diverse human cancers. *Nature.* 2007;447(7147):966–971.
22. Lee JW, et al. Mutational analysis of the hCDC4 gene in gastric carcinomas. *Eur J Cancer.* 2006; 42(14):2369–2373.
23. Kemp Z, et al. CDC4 mutations occur in a subset of colorectal cancers but are not predicted to cause loss of function and are not associated with chromosomal instability. *Cancer Res.* 2005; 65(24):11361–11366.
24. Hubalek MM, et al. Cyclin E dysregulation and chromosomal instability in endometrial cancer. *Oncogene.* 2004;23(23):4187–4192.
25. Koh MS, Ittmann M, Kadmon D, Thompson TC, Leach FS. CDC4 gene expression as potential biomarker for targeted therapy in prostate cancer. *Cancer Biol Ther.* 2006;5(1):78–83.
26. Calhoun ES, et al. BRAF and FBXW7 (CDC4, FBW7, AGO, SEL10) mutations in distinct subsets of pancreatic cancer: potential therapeutic targets. *Am J Pathol.* 2003;163(4):1255–1260.
27. Akhoondi S, et al. FBXW7/hCDC4 is a general tumor suppressor in human cancer. *Cancer Res.* 2007;67(19):9006–9012.
28. Song JH, Schnittke N, Zaat A, Walsh CS, Miller CW. FBXW7 mutation in adult T-cell and B-cell acute lymphocytic leukemias. *Leuk Res.* 2008; 32(11):1751–1755.
29. Thompson BJ, et al. The SCF^{FBW7} ubiquitin ligase complex as a tumor suppressor in T cell leukemia. *J Exp Med.* 2007;204(8):1825–1835.
30. O'Neil J, et al. FBW7 mutations in leukemic cells mediate NOTCH pathway activation and resistance to gamma-secretase inhibitors. *J Exp Med.* 2007;204(8):1813–1824.
31. Malyukova A, et al. The tumor suppressor gene hCDC4 is frequently mutated in human T-cell acute lymphoblastic leukemia with functional consequences for Notch signaling. *Cancer Res.* 2007;67(12):5611–5616.
32. Tsunematsu R, et al. Mouse Fbw7/Sel-10/Cdc4 is required for notch degradation during vascular development. *J Biol Chem.* 2004;279(10):9417–9423.
33. Tetzlaff MT, et al. Defective cardiovascular development and elevated cyclin E and Notch proteins in mice lacking the Fbw7 F-box protein. *Proc Natl Acad Sci U S A.* 2004;101(10):3338–3345.
34. Onoyama I, et al. Conditional inactivation of Fbxw7 impairs cell-cycle exit during T cell differentiation and results in lymphomatogenesis. *J Exp Med.* 2007;204(12):2875–2888.
35. Matsuoka S, et al. Fbxw7 acts as a critical fail-safe against premature loss of hematopoietic stem cells and development of T-ALL. *Genes Dev.* 2008;22(8):986–991.
36. Ishikawa Y, Onoyama I, Nakayama KI, Nakayama K. Notch-dependent cell cycle arrest and apoptosis in mouse embryonic fibroblasts lacking Fbxw7. *Oncogene.* 2008;27(47):6164–6174.
37. Matteoni CA, Younossi ZM, Gramlich T, Boparai N, Liu YC, McCullough AJ. Nonalcoholic fatty liver disease: a spectrum of clinical and pathological

severity. *Gastroenterology*. 1999;116(6):1413–1419.
38. Horton JD, et al. Combined analysis of oligonucleotide microarray data from transgenic and knockout mice identifies direct SREBP target genes. *Proc Natl Acad Sci U S A*. 2003;100(21):12027–12032.
39. Kim BJ, Fulton AB. The genetics and ocular findings of Alagille syndrome. *Semin Ophthalmol*. 2007;22(4):205–210.
40. Loomes KM, et al. Bile duct proliferation in liver-specific Jag1 conditional knockout mice: effects of gene dosage. *Hepatology*. 2007;45(2):323–330.
41. Nishikawa Y, et al. Transdifferentiation of mature rat hepatocytes into bile duct-like cells in vitro. *Am J Pathol*. 2005;166(4):1077–1088.
42. McCright B, Lozier J, Gridley T. A mouse model of Alagille syndrome: Notch2 as a genetic modifier of Jag1 haploinsufficiency. *Development*. 2002;129(4):1075–1082.
43. McDaniell R, et al. NOTCH2 mutations cause Alagille syndrome, a heterogeneous disorder of the notch signaling pathway. *Am J Hum Genet*. 2006; 79(1):169–173.
44. Kodama Y, Hijikata M, Kageyama R, Shimotohno K, Chiba T. The role of notch signaling in the development of intrahepatic bile ducts. *Gastroenterology*. 2004;127(6):1775–1786.
45. Suzuki A, et al. Flow-cytometric separation and enrichment of hepatic progenitor cells in the developing mouse liver. *Hepatology*. 2000;32(6):1230–1239.
46. Leclercq IA, Farrell GC, Schriemer R, Robertson GR. Leptin is essential for the hepatic fibrogenic response to chronic liver injury. *J Hepatol*. 2002;37(2):206–213.
47. Sahai A, et al. Obese and diabetic *db/db* mice develop marked liver fibrosis in a model of nonalcoholic steatohepatitis: role of short-form leptin receptors and osteopontin. *Am J Physiol Gastrointest Liver Physiol*. 2004;287(5):G1035–G1043.
48. Horie Y, et al. Hepatocyte-specific Pten deficiency results in steatohepatitis and hepatocellular carcinomas. *J Clin Invest*. 2004;113(12):1774–1783.
49. Luedde T, et al. Deletion of NEMO/IKKgamma in liver parenchymal cells causes steatohepatitis and hepatocellular carcinoma. *Cancer Cell*. 2007; 11(2):119–132.
50. Isoda K, et al. Deficiency of interleukin-1 receptor antagonist deteriorates fatty liver and cholesterol metabolism in hypercholesterolemic mice. *J Biol Chem*. 2005;280(8):7002–7009.
51. Nakanishi Y, et al. Nonalcoholic steatohepatitis and hepatocellular carcinoma in galectin-3 knockout mice. *Hepatol Res*. 2008;38(12):1241–1251.
52. Yanagitani A, et al. Retinoic acid receptor alpha dominant negative form causes steatohepatitis and liver tumors in transgenic mice. *Hepatology*. 2004;40(2):366–375.
53. Nakayama H, et al. Transgenic mice expressing nuclear sterol regulatory element-binding protein 1c in adipose tissue exhibit liver histology similar to nonalcoholic steatohepatitis. *Metabolism*. 2007;56(4):470–475.
54. Consortium ECTS. Identification and characterization of the tuberous sclerosis gene on chromosome 16. *Cell*. 1993;75(7):1305–1315.
55. van Slegtenhorst M, et al. Identification of the tuberous sclerosis gene TSC1 on chromosome 9q34. *Science*. 1997;277(5327):805–808.
56. Li Z, White P, Tuteja G, Rubins N, Sackett S, Kaestner KH. Foxa1 and Foxa2 regulate bile duct development in mice. *J Clin Invest*. 2009;119(6):1537–1545.
57. Kuhn R, Schwenk F, Aguet M, Rajewsky K. Inducible gene targeting in mice. *Science*. 1995; 269(5229):1427–1429.
58. Postic C, Magnuson MA. DNA excision in liver by an albumin-Cre transgene occurs progressively with age. *Genesis*. 2000;26(2):149–150.
59. Tanigaki K, et al. Regulation of alphabeta/gammadelta T cell lineage commitment and peripheral T cell responses by Notch/RBP-J signaling. *Immunity*. 2004;20(5):611–622.
60. de Alboran IM, et al. Analysis of C-MYC function in normal cells via conditional gene-targeted mutation. *Immunity*. 2001;14(1):45–55.
61. Kamura T, et al. Cytoplasmic ubiquitin ligase KPC regulates proteolysis of $p27^{Kip1}$ at G1 phase. *Nat Cell Biol*. 2004;6(12):1229–1235.
62. Nishiyama M, Nakayama K, Tsunematsu R, Tsukiyama T, Kikuchi A, Nakayama KI. Early embryonic death in mice lacking the beta-catenin-binding protein Duplin. *Mol Cell Biol*. 2004;24(19):8386–8394.
63. Morita S, Kojima T, Kitamura T. Plat-E: an efficient and stable system for transient packaging of retroviruses. *Gene Ther*. 2000;7(12):1063–1066.

LETTER

doi:10.1038/nature09732

SCF^{FBW7} regulates cellular apoptosis by targeting MCL1 for ubiquitylation and destruction

Hiroyuki Inuzuka[1], Shavali Shaik[1]*, Ichiro Onoyama[2]*, Daming Gao[1], Alan Tseng[1], Richard S. Maser[3,4], Bo Zhai[5], Lixin Wan[1], Alejandro Gutierrez[6], Alan W. Lau[1], Yonghong Xiao[3], Amanda L. Christie[6,7], Jon Aster[8], Jeffrey Settleman[9], Steven P. Gygi[5], Andrew L. Kung[6,7], Thomas Look[6], Keiichi I. Nakayama[2], Ronald A. DePinho[3] & Wenyi Wei[1]

The effective use of targeted therapy is highly dependent on the identification of responder patient populations. Loss of *FBW7*, which encodes a tumour-suppressor protein, is frequently found in various types of human cancer, including breast cancer, colon cancer[1] and T-cell acute lymphoblastic leukaemia (T-ALL)[2]. In line with these genomic data, engineered deletion of *Fbw7* in mouse T cells results in T-ALL[3–5], validating FBW7 as a T-ALL tumour suppressor. Determining the precise molecular mechanisms by which FBW7 exerts antitumour activity is an area of intensive investigation. These mechanisms are thought to relate in part to FBW7-mediated destruction of key proteins relevant to cancer, including Jun[6], Myc[7], cyclin E[8] and notch 1 (ref. 9), all of which have oncoprotein activity and are overexpressed in various human cancers, including leukaemia. In addition to accelerating cell growth[10], overexpression of Jun, Myc or notch 1 can also induce programmed cell death[11]. Thus, considerable uncertainty surrounds how FBW7-deficient cells evade cell death in the setting of upregulated Jun, Myc and/or notch 1. Here we show that the E3 ubiquitin ligase SCF^{FBW7} (a SKP1–cullin-1–F-box complex that contains FBW7 as the F-box protein) governs cellular apoptosis by targeting MCL1, a pro-survival BCL2 family member, for ubiquitylation and destruction in a manner that depends on phosphorylation by glycogen synthase kinase 3. Human T-ALL cell lines showed a close relationship between *FBW7* loss and MCL1 overexpression. Correspondingly, T-ALL cell lines with defective FBW7 are particularly sensitive to the multi-kinase inhibitor sorafenib but resistant to the BCL2 antagonist ABT-737. On the genetic level, *FBW7* reconstitution or *MCL1* depletion restores sensitivity to ABT-737, establishing MCL1 as a therapeutically relevant bypass survival mechanism that enables *FBW7*-deficient cells to evade apoptosis. Therefore, our work provides insight into the molecular mechanism of direct tumour suppression by FBW7 and has implications for the targeted treatment of patients with *FBW7*-deficient T-ALL.

MCL1 is frequently overexpressed in various leukaemias through mechanisms that are not fully understood[12]. MCL1 is distinct from other BCL2 family members in its extremely unstable nature[13], which provides a mechanism for cells to switch to either survival or apoptotic mode in response to various stresses[14]. Phosphorylation of MCL1 by glycogen synthase kinase 3 (GSK3) regulates the stability of MCL1 (ref. 13), but little is known about the identity of the E3 ubiquitin ligase that targets phosphorylated MCL1 for destruction. On examination of the GSK3-mediated phosphorylation sites in MCL1, we surmised that they resemble a degron sequence that can be recognized by FBW7 (also known as FBXW7) (Fig. 1a), prompting us to test the possibility that GSK3-mediated phosphorylation of MCL1 triggers the degradation of MCL1 by FBW7. Depletion of FBW7 (Fig. 1b) or the SCF components cullin 1 (CUL1), RBX1 and SKP1 (Fig. 1c), but not other F-box proteins that we examined (Fig. 1b), resulted in a significant increase in the amount of MCL1 protein. T-cell-lineage-specific depletion of FBW7 in *Fbw7* conditional knockout (Lck-Cre/$Fbw7^{fl/fl}$)mice[3] resulted in increased MCL1 levels in the thymuses of these mice (Fig. 1d), as well as thymic lymphoma (Supplementary Fig. 1a) and the presence of acute leukaemia cells in the thymuses (Supplementary Fig. 1b). Consistent with a recent study[15], $FBW7^{-/-}$ human DLD1 cells (Fig. 1e) and HeLa cells treated with short interfering RNA (siRNA) directed against *FBW7* (Supplementary Fig. 1c) have elevated MCL1 expression mainly in the mitosis (M) and early G1 phases of the cell cycle.

The clinical relevance of this finding is further demonstrated by the finding that human T-ALL cell lines harbouring *FBW7* mutations and/or deletions have a significant increase in MCL1 (Fig. 1f). Additionally, depletion of FBW7 in DND41 cells or Loucy cells (both of which have wild-type *FBW7*) leads to increased MCL1 expression (Fig. 1g), whereas reintroduction of wild-type *FBW7* dramatically reduced MCL1 expression in FBW7-deficient T-ALL cells (Fig. 1h), supporting a causal relationship between loss of FBW7 activity and elevated MCL1 expression in the T-ALL cells examined. More importantly, elevated MCL1 expression is also observed in both primary human and mouse T-ALL samples with deficient FBW7 activity[2–4] (Fig. 1i, j and Supplementary Fig. 1a, b), and depletion of MCL1 impaired T-ALL disease progression *in vivo* (Fig. 1k–m).

Consistent with a post-translational mode of regulation, no changes in *MCL1* mRNA levels were observed after depletion of FBW7 in DLD1 cells (Supplementary Fig. 2d), and no positive relationship was observed between *MCL1* mRNA levels and loss of *FBW7* in T-ALL cells (Supplementary Fig. 2e). The half-life of MCL1 was significantly extended in the thymuses of $Fbw7^{-/-}$ mice and FBW7-deficient human T-ALL cells (Supplementary Fig. 3a–c), and experimental manipulation of FBW7 levels changed MCL1 stability accordingly (Supplementary Fig. 3d, e). Together, these results suggest that MCL1 is a downstream ubiquitylation target of SCF^{FBW7}.

As the proper substrate phosphorylation events are required for FBW7 to recognize and target its substrates for ubiquitylation[16], we next investigated which phosphorylation events trigger MCL1 destruction by FBW7. Mass spectrometry analysis showed that MCL1 is phosphorylated at multiple sites *in vivo* (Fig. 2a and Supplementary Fig. 5a–c). In addition to serine at position 159 (S159) and threonine at position 163 (T163)[13,17], S64 and S121 were also phosphorylated *in vivo*. Consistent with previous reports[13,17], MCL1 destruction is promoted by GSK3 (Fig. 2b) but not by the protein kinases ERK1 (also

[1]Department of Pathology, Beth Israel Deaconess Medical Center, Harvard Medical School, 330 Brookline Avenue, Boston, Massachusetts 02215, USA. [2]Department of Molecular and Cellular Biology, Medical Institute of Bioregulation, Kyushu University, Fukuoka, Fukuoka 812-8582, Japan. [3]Belfer Institute for Applied Cancer Science, Department of Medical Oncology, Dana-Farber Cancer Institute, Harvard Medical School, Boston, Massachusetts 02115, USA. [4]The Jackson Laboratory, Bar Harbor, Maine 04609, USA. [5]Department of Cell Biology, Harvard Medical School, Boston, Massachusetts 02115, USA. [6]Department of Pediatric Oncology, Dana-Farber Cancer Institute, Harvard Medical School, Boston, Massachusetts 02115, USA. [7]Lurie Family Imaging Center, Dana-Farber Cancer Institute, Boston, Massachusetts 02115, USA. [8]Department of Pathology, Brigham and Women's Hospital, Harvard Medical School, Boston, Massachusetts 02115, USA. [9]Department of Medicine, Massachusetts General Hospital Cancer Center, Harvard Medical School, Charlestown, Massachusetts 02129, USA.
*These authors contributed equally to this work.

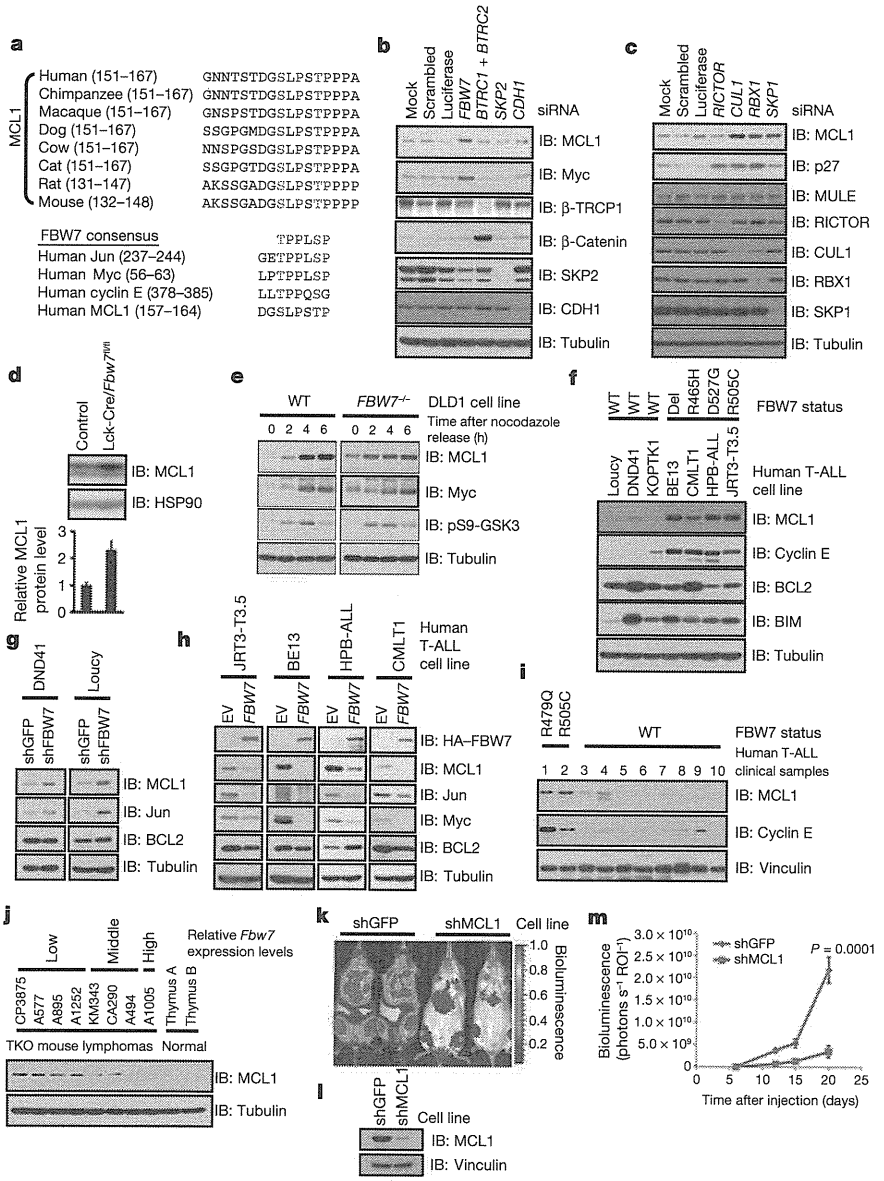

Figure 1 | MCL1 stability is controlled by FBW7. **a**, Sequence alignment of MCL1 with the phosphodegron sequences recognized by FBW7 in Jun, Myc and cyclin E. The putative FBW7 phosphodegron sequence present in MCL1 is conserved across different species. Conserved serine and threonine residues within the degron sequences are shown in red, and conserved proline residues are shown in blue. **b**, **c**, Immunoblotting (IB) analysis, with antibodies specific for the indicated proteins (right), of HeLa cells transfected with siRNA oligonucleotides directed against the indicated genes (top). **d**, IB analysis of thymocytes derived from control (Lck-Cre/*Fbw7*$^{+/fl}$) mice or *Fbw7* conditional knockout (Lck-Cre/*Fbw7*$^{fl/fl}$) mice (whose thymocytes lack *Fbw7*). For the histogram, MCL1 band intensity was normalized to HSP90 and then normalized to the control lane. Data are shown as mean ± s.e.m. for three independent experiments. **e**, IB analysis of wild-type (WT) and *FBW7*$^{-/-}$ DLD1 cells after synchronization of the cell cycles with nocodazole and release from mitotic arrest at the indicated time points. pS9-GSK3, GSK3 that is phosphorylated at the S9 residue. **f**, IB analysis of the indicated human T-ALL cell lines, which have either WT FBW7 or mutant FBW7 (a deletion (Del) or an amino acid substitution). **g**, The human T-ALL cell lines DND41 and Loucy cells, which contain wild-type *FBW7*, were infected with the indicated lentiviral shRNA constructs and selected with 1 μg ml^{-1} puromycin to eliminate the non-infected cells. Cell lysates were collected for IB analysis. shFBW7, shRNA specific for *FBW7*; shGFP, shRNA specific for the gene encoding green fluorescent protein (GFP). **h**, Human T-ALL cell lines deficient in FBW7 were infected with an *FBW7*-expressing retroviral construct (with empty vector (EV) as a negative control) and selected with 1 μg ml^{-1} puromycin to eliminate the non-infected cells. Cell lysates were collected for IB analysis. HA, haemagglutinin tag. **i**, IB analysis of the indicated primary human T-ALL clinical samples. **j**, IB analysis of the indicated mouse T-ALL cell lines derived from *Terc*$^{-/-}$*Atm*$^{-/-}$*Tp53*$^{-/-}$ (TKO) mice. **k**–**m**, *In vivo* effects of MCL1 depletion in FBW7-deficient T-ALL cells. An *in vivo* model of FBW7-deficient T-ALL was created by orthotopic engraftment of luciferase-expressing CMLT1 cells in immunodeficient (NOD SCID *Il2rg*-null) mice. Mice were injected with 1×10^7 cells ($n = 7$ per group) through the lateral tail vein. Before engraftment, cells were infected with retroviral constructs expressing the indicated shRNAs. **k**, Representative images of luciferase expression (photonic flux, in number of photons s^{-1} cm^{-2} sr^{-1} × 10^6) detected in live mice, which had received CMLT1–shGFP (left) or CMLT1–shMCL1 (right). **l**, IB analysis of the engineered CMLT1 cell lines, showing the efficient depletion of MCL1. **m**, Tumour burden was determined by quantification of total body luminescence and is expressed as photons s^{-1} ROI^{-1}. Data are presented as mean ± s.e.m., with statistical significance determined by Student's *t*-test.

known as MAPK3) and/or ERK2 (also known as MAPK1) (Supplementary Fig. 5d–f). To investigate further the significance of each individual phosphorylation site, we created a panel of MCL1 mutants (Fig. 2c). Using *in vitro* kinase assays, we identified S159 and T163 as the major GSK3-mediated phosphorylation sites[17] and S121 as a minor GSK3-mediated phosphorylation site (Fig. 2d, e and Supplementary

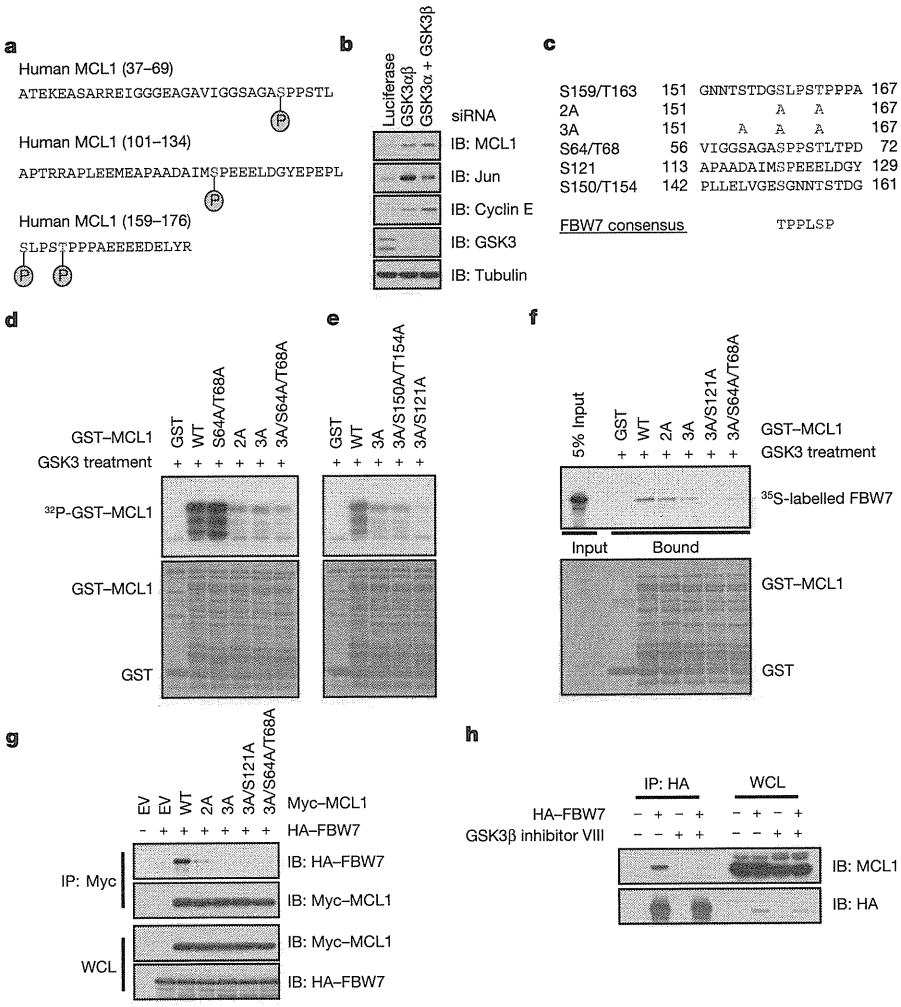

Figure 2 | Phosphorylation of MCL1 by GSK3 triggers the interaction of MCL1 with FBW7. a, *In vivo* MCL1 phosphorylation sites detected by mass spectrometry analysis. Phosphorylated residues are shown in red, with phosphate in blue. **b**, IB analysis, with antibodies specific for the indicated proteins (right), of HeLa cells transfected with siRNA oligonucleotides directed against the indicated genes (top) (where GSK3αβ indicates depletion of *GSK3A* and *GSK3B* with a single siRNA and GSK3α + GSK3β indicates depletion with siRNAs targeting each gene separately). **c**, Illustration of the various MCL1 mutants generated for this study. Conserved serine and threonine residues within the degron sequence are shown in red, and conserved proline residues are shown in blue. 2A, MCL1 S159A/T163A; 3A, MCL1 S155A/S159A/T163A. **d**, **e**, GSK3 phosphorylates MCL1 *in vitro* at multiple sites. Purified GSK3 protein was incubated with 5 μg of the indicated glutathione *S*-transferase (GST)–MCL1 fusion proteins (top, WT and mutant as in **c**) in the presence of [γ-^{32}P]ATP. The protein kinase reaction products were resolved by SDS–PAGE, and phosphorylation was detected by autoradiography. **f**, Phosphorylation of MCL1 at multiple sites by GSK3 triggers the interaction of MCL1 with FBW7 *in vitro*. Autoradiograms show recovery of ^{35}S-labelled FBW7 protein bound to the indicated GST–MCL1 fusion proteins (with GST protein as a negative control) incubated with GSK3 before the pull-down assays. **g**, IB analysis of whole-cell lysates (WCL) and immunoprecipitates (IP) derived from 293T cells transfected with HA–FBW7 together with the indicated Myc–MCL1 constructs (top). Thirty hours after transfection, cells were pretreated with 10 μM MG132 for 10 h to block the proteasome pathway before cell collection. **h**, IB analysis of WCL and IP derived from 293T cells transfected with HA–FBW7. Thirty hours after transfection, cells were pretreated with 20 μM MG132 for 8 h to block the proteasome pathway before cell collection. Where indicated, 25 μM GSK3β inhibitor VIII (with dimethylsulphoxide (DMSO) as a negative control) was added for 8 h before cell collection.

Fig. 5g). Inactivation of these GSK3-mediated phosphorylation sites impairs the interaction between MCL1 and FBW7 both *in vitro* (Fig. 2f and Supplementary Fig. 5h) and *in vivo* (Fig. 2g and Supplementary Fig. 5i). Furthermore, pharmacological inhibition of GSK3 activity blocked the interaction between HA-tagged FBW7 and endogenous MCL1 (Fig. 2h) and inhibited the localization of FBW7 to the mitochondria, where MCL1 resides (Supplementary Fig. 5j, k). These results indicate that GSK3-dependent phosphorylation of MCL1 is necessary for the interaction of MCL1 with FBW7. Consistent with this FBW7–MCL1 regulatory axis, MCL1 specifically interacts with FBW7 (Supplementary Fig. 6a, b, j–l) and CUL1 (Supplementary Fig. 6c, d), and depletion of endogenous CUL1 increases MCL1 abundance (Supplementary Fig. 11a).

We next explored the mechanism by which FBW7 alters MCL1 stability. Overexpression of FBW7 and GSK3 significantly decreased MCL1 abundance (Fig. 3a and Supplementary Fig. 6h), whereas inactivation of the major GSK3-dependent phosphorylation sites on MCL1 impaired FBW7-mediated destruction (Fig. 3b and Supplementary Fig. 6e–g). All FBW7 isoforms (particularly the α-isoform and the γ-isoform) participate in MCL1 stability control, and FBW7 dimerization is not required for the degradation of MCL1 (Supplementary Fig. 7a–e). Mutant FBW7 constructs derived from patients with T-ALL showed a reduced ability to interact with MCL1 (Supplementary Fig. 6i) and were therefore unable to degrade MCL1 (Fig. 3c). Moreover, the FBW7- and GSK3-mediated destruction of MCL1 was blocked by the proteasome inhibitor MG132, indicating the involvement of the ubiquitin–proteasome pathway in this process (Fig. 3a). In support of this idea, co-expression of GSK3 and FBW7 resulted in a marked reduction in the half-life of wild-type MCL1, but not of the 2A or 3A MCL1 mutants (Fig. 3d), with reduced interaction with FBW7

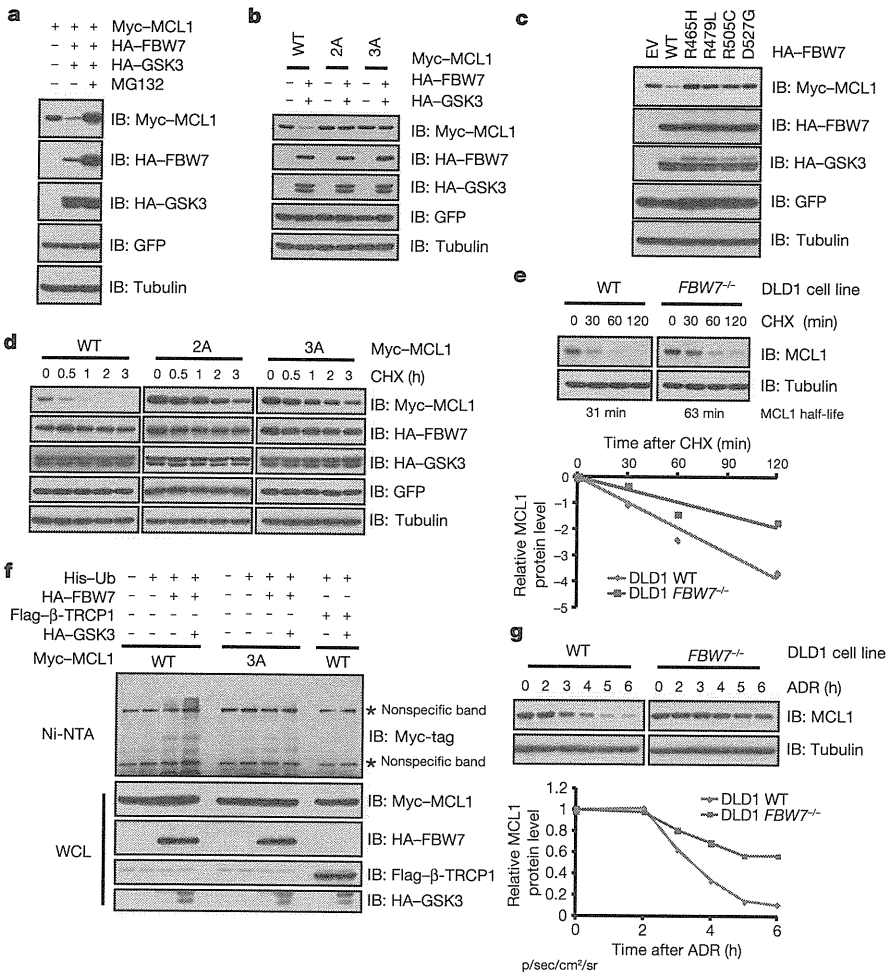

Figure 3 | FBW7 promotes MCL1 ubiquitylation and destruction in a GSK3-mediated phosphorylation-dependent manner. a–c, GSK3-mediated phosphorylation-dependent degradation of MCL1 by FBW7. IB analysis of 293T cells transfected with plasmids expressing the indicated Myc–MCL1 and HA–FBW7 proteins in the presence or absence of HA–GSK3 (top), with antibodies specific for the Myc tag, HA tag, GFP or tubulin (right). A plasmid encoding GFP was used as a negative control for transfection efficiency. Where indicated, the proteasome inhibitor MG132 was added. **d**, 293T cells were transfected with the indicated Myc–MCL1 constructs together with the HA–FBW7- and HA–GSK3-expressing plasmids. Twenty hours after transfection, cells were split into 60-mm dishes. After another 20 h, cells were treated with 20 μg ml^{-1} cycloheximide (CHX). At the indicated time points, WCL were prepared, and IB analysis was carried out with antibodies specific for the indicated proteins. **e**, Top, WT or *FBW7*$^{-/-}$ DLD1 cells were treated with 20 μg ml^{-1} CHX. At the indicated time points, WCL were prepared, and IB analysis was carried out with antibodies specific for the indicated proteins. Bottom, MCL1 band intensity was normalized to tubulin and then normalized to the $t = 0$ controls. **f**, IB of WCL and His tag pull-down of HeLa cells transfected with plasmids expressing the indicated proteins. Twenty hours after transfection, cells were treated with the proteasome inhibitor MG132 for 12 h before cell collection. His tag pull-down was performed in the presence of 8 M urea to eliminate any possible contamination from MCL1-associated proteins. Ni-NTA, nickel-nitrilotriacetic acid; Ub, ubiquitin. **g**, Top, IB analysis of WT and *FBW7*$^{-/-}$ DLD1 cells treated with 10 μM adriamycin (ADR) for the indicated time durations. Bottom, MCL1 band intensity was normalized to tubulin and then normalized to the $t = 0$ controls.

(Fig. 2g). Furthermore, loss of *FBW7* extends the half-life of endogenous MCL1 (Fig. 3e), and FBW7 promotes the ubiquitylation of MCL1 in a GSK3-dependent manner (Fig. 3f and Supplementary Fig. 8a, b, e). The decrease of MCL1 expression is also impaired in response to various DNA-damaging agents[18] in *FBW7*$^{-/-}$ DLD1 cells (Fig. 3g and Supplementary Fig. 8f). Together, these data suggest a physiological role for FBW7 in promoting MCL1 destruction *in vivo* in a GSK3-mediated phosphorylation-dependent manner.

Next, we explored how FBW7 affects the cellular apoptotic response by modulating MCL1 abundance. As predicted, *Fbw7*$^{-/-}$ mouse thymocytes and FBW7-deficient human T-ALL cells with increased MCL1 levels were less sensitive to apoptotic stimuli (Supplementary Fig. 9a–f). More interestingly, compared with T-ALL cell lines that had wild-type *FBW7*, FBW7-deficient T-ALL cells with elevated MCL1 expression (Fig. 1f and Supplementary Fig. 9h) were more sensitive to the multi-kinase inhibitor sorafenib, which can effectively reduce MCL1 expression[19,20] (Fig. 4a and Supplementary Fig. 9g–i). Although the ability of sorafenib to repress MCL1 has been attributed to the inactivation of the RAF–ERK pathway and/or the activation of GSK3 activity[19], the exact mechanism remains unclear. Nonetheless, these data suggest that FBW7-deficient T-ALL cell lines might require elevated levels of MCL1 to evade apoptosis, a phenotype known as 'oncogene addiction'[21]. By contrast, FBW7-deficient T-ALL cell lines were more resistant to ABT-737 (Fig. 4a and Supplementary Fig. 9g, j). ABT-737 is a BH3 domain mimetic and a pan inhibitor of the BCL2 family of anti-apoptotic proteins, and it is reported to kill leukaemia cells effectively[22]. However, leukaemia cells with elevated MCL1 levels are refractory to treatment with ABT-737 (refs 23, 24), primarily because ABT-737 fails to inactivate MCL1 (ref. 22). Experimental evidence from both double staining with 7-amino-actinomycin D (7-AAD) and annexin V (Supplementary Fig. 9j) and immunoblotting specific for apoptotic biomarkers (Fig. 4b) suggests that ABT-737-induced apoptosis is impaired in FBW7-deficient T-ALL cells. Moreover, specific depletion of MCL1 in multiple FBW7-deficient T-ALL cell lines restored the sensitivity of these cells to ABT-737 (Fig. 4c, d), supporting the idea that increased MCL1 expression is

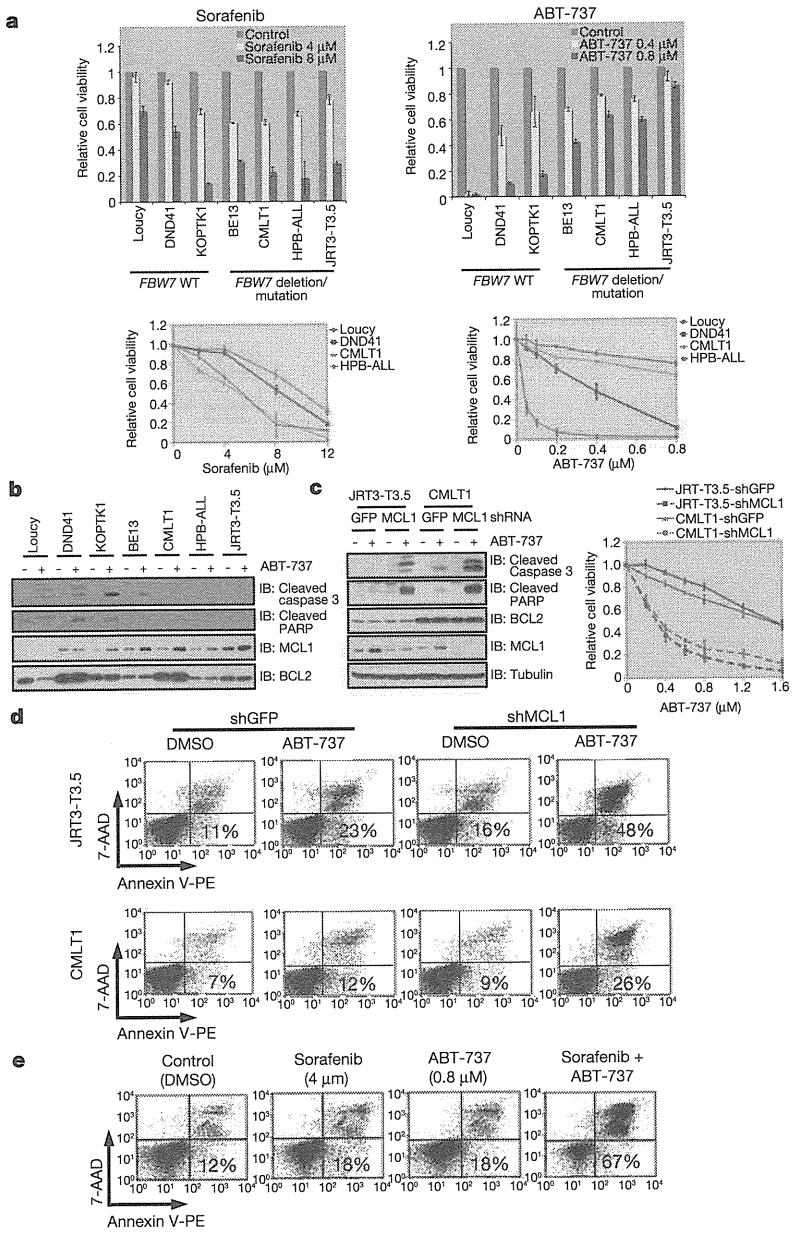

Figure 4 | Elevated MCL1 expression protects FBW7-deficient T-ALL cell lines from ABT-737-induced apoptosis. **a**, Cell viability assays showing that FBW7-deficient human T-ALL cell lines were more sensitive to sorafenib but were relatively resistant to ABT-737 treatment. T-ALL cells were cultured in 10% FBS-containing medium with the indicated concentrations of sorafenib or ABT-737 for 48 h before cell viability assays were performed. Data are shown as mean ± s.d. for three independent experiments. **b**, IB analysis of the indicated human T-ALL cell lines with or without ABT-737 (0.8 μM) treatment. PARP, poly(ADP-ribose) polymerase. **c**, Specific depletion of endogenous MCL1 expression restored sensitivity to ABT-737 in the indicated FBW7-deficient human T-ALL cell lines. Various T-ALL cell lines were infected with lentiviral shGFP- or shMCL1-encoding vectors and selected in 0.5 μg ml^{-1} puromycin to eliminate non-infected cells. The generated cell lines were cultured in 10% FBS-containing medium with the indicated concentrations of ABT-737 for 48 h before cell viability assays were performed (right) or with or without ABT-737 (0.8 μM) treatment for 24 h before WCL were collected for IB analysis with antibodies specific for the indicated proteins (left). For cell viability assays, data are shown as mean ± s.d. for three independent experiments. **d**, Double staining with 7-AAD and annexin-V–PE (annexin V conjugated to phycoerythrin), followed by flow cytometry analysis to detect the percentage of apoptotic cells (axes indicate intensity of fluorochrome). In the indicated FBW7-deficient human T-ALL cell lines, endogenous MCL1 was depleted by infection with lentiviral vectors encoding shRNA (lentiviral shGFP was used as a negative control). Cell lines were cultured in 10% FBS-containing medium with or without ABT-737 (0.8 μM) treatment, with DMSO as a negative control, for 48 h before the flow cytometry analysis. Purple numbers indicate the percentage of apoptotic cells. **e**, Staining and flow cytometry analysis as in **d**, demonstrating that sorafenib treatment restores ABT-737 sensitivity to FBW7-deficient HPB-ALL cells. HPB-ALL cells were cultured in 10% FBS-containing medium with the indicated concentrations of sorafenib and/or ABT-737 for 48 h before analysis. Coloured numbers indicate the percentage of apoptotic cells.

the primary cause of desensitization to ABT-737 *in vivo*[23,24]. It also suggests that patients with FBW7-deficient T-ALL will not respond well to treatment with ABT-737. We further demonstrated that manipulation of FBW7 activity or ectopic expression of a non-degradable form of MCL1 in human T-ALL cells affects their sensitivity to ABT-737 (Supplementary Fig. 10a, b) and responses to other apoptotic stimuli (Supplementary Fig. 10c–f).

Our results indicate that inhibition of MCL1 could be used to restore sensitivity to ABT-737 in FBW7-deficient T-ALL cells. Given that the clinical application of siRNA- or short hairpin RNA (shRNA)-mediated target extinction is not yet feasible owing to delivery challenges, we instead exploited small molecule strategies to reduce MCL1 expression, specifically with the use of sorafenib (Supplementary Fig. 9h). The combined use of sorafenib and ABT-737 produced a dose-dependent

increase in the sensitivity of HPB-ALL cells, a human T-ALL cell line, to ABT-737 (Supplementary Fig. 10g), and this decrease correlated with a significant increase in the induction of apoptosis (Fig. 4e). Similar results were obtained for other FBW7-deficient T-ALL cell lines (Supplementary Fig. 10h).

Our studies provide experimental evidence of a role for FBW7 in governing the apoptotic pathway by controlling MCL1 destruction. MCL1 has a key role in regulating the apoptosis of T cells[14] but not of cells from other tissue types, such as liver cells. Therefore, our studies also provide a possible mechanistic explanation for why loss of *FBW7* is frequently seen in patients with T-ALL. Although other E3 ubiquitin ligases, including MULE[25] and β-transducin-repeat-containing protein (β-TRCP)[17], have been implicated in controlling MCL1 stability, MULE activity was not implicated in the GSK3-dependent regulation of MCL1 (refs 17, 25) (Supplementary Fig. 11a–e). Additionally, no correlation was found between MULE and MCL1 expression in various T-ALL cells (Supplementary Fig. 11f), thereby excluding a physiological role for MULE in regulating MCL1 abundance in T-ALL cells. We further found that depletion of FBW7, but not β-TRCP, leads to a significant induction of MCL1 expression (Fig. 1b and Supplementary Fig. 11a–c). Array comparative genomic hybridization analysis demonstrated a high frequency of *FBW7* loss[2] but not simultaneous loss of *BTRC1* and *BTRC2*, which encode β-TRCPs, in T-ALL cells (data not shown). Together, these data support the hypothesis that SCF^{FBW7} is a physiological E3 ubiquitin ligase for MCL1, with USP9X being the nominated deubiquitylase[26], and that loss of *FBW7* contributes to T-ALL development through the upregulation of MCL1 expression. More importantly, our studies suggest that there is a correlation between *FBW7* genetic status and sensitivity to ABT-737, and they provide insight into the use of MCL1 inhibitors as a practical method for specifically killing FBW7-deficient T-ALL cells. This work provides a basis for the rational treatment of patients with T-ALL and provides motivation for the development of specific MCL1 antagonists, or agents that significantly reduce MCL1 expression, for the improved management of patients with T-ALL.

METHODS SUMMARY

Expression plasmid constructs, proteins, antibodies and cell lines are described in the Methods. The sequences of various siRNA oligonucleotides used in this study are also listed in the Methods. *In vivo* phosphorylation of MCL1 was detected by mass spectrometry analysis, and the major GSK3-dependent phosphorylation sites that were identified were subsequently examined by *in vitro* kinase assays. All mutants were generated using PCR, and the sequences were verified. FBW7-mediated MCL1 ubiquitylation and destruction were examined by cell-based ubiquitylation and degradation assays. Cell viability assays were used to detect the response of various T-ALL cell lines to sorafenib and ABT-737. Double staining with annexin V and 7-AAD was used to detect the percentage of apoptotic cells.

Full Methods and any associated references are available in the online version of the paper at www.nature.com/nature.

Received 12 October 2009; accepted 29 November 2010.

1. Wood, L. D. *et al.* The genomic landscapes of human breast and colorectal cancers. *Science* **318,** 1108–1113 (2007).
2. Maser, R. S. *et al.* Chromosomally unstable mouse tumours have genomic alterations similar to diverse human cancers. *Nature* **447,** 966–971 (2007).
3. Onoyama, I. *et al.* Conditional inactivation of *Fbxw7* impairs cell-cycle exit during T cell differentiation and results in lymphomatogenesis. *J. Exp. Med.* **204,** 2875–2888 (2007).
4. Matsuoka, S. *et al.* Fbxw7 acts as a critical fail-safe against premature loss of hematopoietic stem cells and development of T-ALL. *Genes Dev.* **22,** 986–991 (2008).
5. Thompson, B. J. *et al.* The SCF^{FBW7} ubiquitin ligase complex as a tumor suppressor in T cell leukemia. *J. Exp. Med.* **204,** 1825–1835 (2007).
6. Wei, W., Jin, J., Schlisio, S., Harper, J. W. & Kaelin, W. G. Jr. The v-Jun point mutation allows c-Jun to escape GSK3-dependent recognition and destruction by the Fbw7 ubiquitin ligase. *Cancer Cell* **8,** 25–33 (2005).
7. Welcker, M. *et al.* The Fbw7 tumor suppressor regulates glycogen synthase kinase 3 phosphorylation-dependent c-Myc protein degradation. *Proc. Natl Acad. Sci. USA* **101,** 9085–9090 (2004).
8. Koepp, D. M. *et al.* Phosphorylation-dependent ubiquitination of cyclin E by the SCF^{Fbw7} ubiquitin ligase. *Science* **294,** 173–177 (2001).
9. Gupta-Rossi, N. *et al.* Functional interaction between SEL-10, an F-box protein, and the nuclear form of activated Notch1 receptor. *J. Biol. Chem.* **276,** 34371–34378 (2001).
10. Shaulian, E. & Karin, M. AP-1 as a regulator of cell life and death. *Nature Cell Biol.* **4,** E131–E136 (2002).
11. Sanchez, I. & Yuan, J. A convoluted way to die. *Neuron* **29,** 563–566 (2001).
12. Akgul, C. Mcl-1 is a potential therapeutic target in multiple types of cancer. *Cell. Mol. Life Sci.* **66,** 1326–1336 (2009).
13. Maurer, U., Charvet, C., Wagman, A. S., Dejardin, E. & Green, D. R. Glycogen synthase kinase-3 regulates mitochondrial outer membrane permeabilization and apoptosis by destabilization of MCL-1. *Mol. Cell* **21,** 749–760 (2006).
14. Opferman, J. T. *et al.* Development and maintenance of B and T lymphocytes requires antiapoptotic MCL-1. *Nature* **426,** 671–676 (2003).
15. Wertz, I. E. *et al.* Sensitivity to antitubulin chemotherapeutics is regulated by MCL1 and FBW7. *Nature* doi:10.1038/nature09779 (this issue).
16. Welcker, M. & Clurman, B. E. FBW7 ubiquitin ligase: a tumour suppressor at the crossroads of cell division, growth and differentiation. *Nature Rev. Cancer* **8,** 83–93 (2008).
17. Ding, Q. *et al.* Degradation of Mcl-1 by β-TrCP mediates glycogen synthase kinase 3-induced tumor suppression and chemosensitization. *Mol. Cell. Biol.* **27,** 4006–4017 (2007).
18. Nijhawan, D. *et al.* Elimination of Mcl-1 is required for the initiation of apoptosis following ultraviolet irradiation. *Genes Dev.* **17,** 1475–1486 (2003).
19. Panka, D. J., Cho, D. C., Atkins, M. B. & Mier, J. W. GSK-3β inhibition enhances sorafenib-induced apoptosis in melanoma cell lines. *J. Biol. Chem.* **283,** 726–732 (2008).
20. Yu, C. *et al.* The role of Mcl-1 downregulation in the proapoptotic activity of the multikinase inhibitor BAY 43-9006. *Oncogene* **24,** 6861–6869 (2005).
21. Sharma, S. V. & Settleman, J. Oncogene addiction: setting the stage for molecularly targeted cancer therapy. *Genes Dev.* **21,** 3214–3231 (2007).
22. Cragg, M. S., Harris, C., Strasser, A. & Scott, C. L. Unleashing the power of inhibitors of oncogenic kinases through BH3 mimetics. *Nature Rev. Cancer* **9,** 321–326 (2009).
23. Konopleva, M. *et al.* Mechanisms of antileukemic activity of the novel Bcl-2 homology domain-3 mimetic GX15-070 (obatoclax). *Cancer Res.* **68,** 3413–3420 (2008).
24. van Delft, M. F. *et al.* The BH3 mimetic ABT-737 targets selective Bcl-2 proteins and efficiently induces apoptosis via Bak/Bax if Mcl-1 is neutralized. *Cancer Cell* **10,** 389–399 (2006).
25. Zhong, Q., Gao, W., Du, F. & Wang, X. Mule/ARF-BP1, a BH3-only E3 ubiquitin ligase, catalyzes the polyubiquitination of Mcl-1 and regulates apoptosis. *Cell* **121,** 1085–1095 (2005).
26. Schwickart, M. *et al.* Deubiquitinase USP9X stabilizes MCL1 and promotes tumour cell survival. *Nature* **463,** 103–107 (2010).

Supplementary Information is linked to the online version of the paper at www.nature.com/nature.

Acknowledgements We thank J. Lawler, C. Schorl, Q. Zhang and S. Glueck for critical reading of the manuscript, J. DeCaprio, M.-C. Hung, M. A. Kelliher, W. Harper and W. Hahn for providing reagents, L. Cantley and A. Toker for suggestions, I. Wertz and V. Dixit for sharing unpublished data, and members of the Wei and DePinho labs for useful discussions. W.W. is a Kimmel Scholar and V Scholar. This work was supported in part by the Emerald Foundation New Investigator award (W.W.), the Leukemia and Lymphoma Society Special Fellow award (W.W.) and a grant from the National Institutes of Health (W.W.; GM089763). R.A.D. is an American Cancer Society Research Professor and is supported by the Robert A. and Renée E. Belfer Foundation Institute for Applied Cancer Science.

Author Contributions H.I. performed most of the experiments with critical assistance from S.S. and D.G. A.T., L.W. and A.W.L. also helped perform a portion of the experiments. I.O. performed the *Fbw7* conditional knockout mouse experiments, and A.L.C. performed the orthotopic engraftment mouse experiments. B.Z. performed the mass spectrometry analysis, and Y.X. and R.S.M. helped to perform the experiments with tumours derived from the TKO mice. A.G. helped to perform the experiments with the human T-ALL clinical samples. W.W., R.A.D. and K.I.N. designed the experiments with assistance from J.A., J. S., A.L.K., H.I., S.P.G. and T.L. W.W. supervised the study. W.W. wrote the manuscript with help from H.I. and S.S. All authors commented on the manuscript.

Author Information Reprints and permissions information is available at www.nature.com/reprints. The authors declare no competing financial interests. Readers are welcome to comment on the online version of this article at www.nature.com/nature. Correspondence and requests for materials should be addressed to W.W. (wwei2@bidmc.harvard.edu).

METHODS

Plasmids. HA–FBW7 and HA–GSK3 constructs were described previously[6]. Human *FBW7* cDNA was subcloned using Pfu polymerase (Stratagene) into the pBabe-Puro-HA retrovirus vector. Myc–MCL1 WT, Myc–MCL1 3A, and GST–MCL1 WT constructs were gifts from M.-C. Hung. FBW7 and MCL1 mutants were generated with the QuikChange XL Site-Directed Mutagenesis Kit (Stratagene) according to the manufacturer's instructions. HA–ERK1, shERK1 and shERK2 constructs were gifts from J. Blenis. Flag–β-TRCP1, Flag–Ub, shTRCP1 and shTRCP1+2 retroviral constructs were gifts from W. Harper. The shFBW7 retroviral vector (Addgene) was validated and described previously[27]. To generate the lentiviral shFBW7 and shMULE vectors, DNA oligonucleotides encoding shRNA directed against FBW7 and MULE were annealed and subcloned into AgeI and EcoRI sites of the pLKO lentiviral plasmid. The following are DNA oligonucleotide sequences for the *FBW7*-directed shRNA (sense, 5′-CCGGAACCTTCTCTGGAGAGAGAAACTCGAGTTTCTCTCTCCAGAGAAGGTTTTTTTG-3′; antisense, 5′-AATTCAAAAAAACCTTCTCTGGAGAGAGAAACTCGAGTTTCTCTCTCCAGAGAAGGTT-3′), and for MULE-directed shRNA (sense, 5′-CCGGAATTGCTATGTCTCTGGGACACTCGAGTGTCCCAGAGACATAGCAATTTTTTTG-3′; antisense, 5′-AATTCAAAAAAATTGCTATGTCTCTGGGACACTCGAGTGTCCCAGAGACATAGCAATT-3′). Lentiviral shRNA constructs against GFP and MCL1 were obtained from W. Hahn. WT *MCL1* and 3A *MCL1* cDNAs were amplified with PCR and subcloned into the BamHI and SalI sites of the pLenti-GFP-Puro construct (Addgene, catalogue number 658-5).

Antibodies and reagents. Anti-Myc antibody (catalogue number sc-40), polyclonal anti-HA antibody (SC-805), anti-cyclin A antibody (SC-751), anti-PLK1 antibody (SC-17783), anti-CUL1 antibody (sc-70895), anti-RICTOR antibody (sc-81538), anti-p27 antibody (sc-528), anti-SKP1 antibody (sc-7163), anti-MCL1 antibody (sc-819) and anti-cyclin E antibody (SC-247) were purchased from Santa Cruz Biotechnology. Anti-tubulin antibody (T-5168), polyclonal anti-Flag antibody (F2425), monoclonal anti-Flag antibody (F-3165), anti-β-catenin antibody (C7207), anti-vinculin antibody (V9131), peroxidase-conjugated anti-mouse secondary antibody (A4416) and peroxidase-conjugated anti-rabbit secondary antibody (A4914) were purchased from Sigma. Anti-MCL1 antibody (4572), anti-BCL2 antibody (2872), anti-COX IV antibody (4850), anti-cleaved caspase 3 (Asp175) antibody (9661), anti-cleaved PARP (Asp214) antibody (9541), anti-ERK1/2 antibody (4695), anti-Jun antibody (9162), anti-phospho-GSK3β (Ser9) antibody (9336) and anti-BIM antibody (4582) were purchased from Cell Signaling Technology. Anti-MULE antibody (A300-486A) was purchased from Bethyl. Monoclonal anti-HA antibody (MMS-101P) was purchased from Covance. Anti-RBX1 antibody (RB-069P1) was purchased from NeoMarker. Another anti-MCL1 antibody (559027) was purchased from BD Pharmingen. Anti-GFP antibody (632380) and another anti-CUL1 antibody (32-2400) were purchased from Invitrogen. Anti-CDH1 antibody (CC43) was purchased from Oncogene. Oligofectamine, Lipofectamine and Plus reagents were purchased from Invitrogen. GSK3β inhibitor VIII was purchased from Calbiochem.

siRNAs. Human siRNA oligonucleotides directed against *FBW7*, *SKP2*, *CDH1* and *CUL1* have been described previously[6,28,29]. A human siRNA oligonucleotide that can deplete both β-TRCP1 and β-TRCP2 (sense, 5′-AAGUGGAAUUUGUGGAACAUC-3′) was purchased from Dharmacon. Human siRNA oligonucleotides directed against MULE (MULE-A: sense, 5′-CAUGCCGCAAUCCAGACAUAU-3′)[25] and (MULE-B: sense, 5′-AAUUGCUAUGUCUCUGGGACA-3′)[30] have been validated previously and were purchased from Dharmacon. Luciferase GL2 siRNA oligonucleotide was purchased from Dharmacon. siRNA oligonucleotides to deplete endogenous RBX1 (sense, 5′-AACUGUGCCAUCUGCAGGAACAA-3′), CUL1 (sense, 5′-GGUCGCUUCAUAAACAACAUU-3′) and RICTOR (sense, 5′-AAACUUGUGAAGAAUCGUAUCUU-3′) were synthesized by Dharmacon. Cocktailed siRNAs targeting *SKP1* were purchased from Invitrogen (1299003). A GSK3α-depleting siRNA oligonucleotide (6312) and a GSK3α/β-depleting siRNA oligonucleotide (6301) were purchased from Cell Signaling Technology. The GSK3β-depleting siRNA oligonucleotide (51012) was purchased from Ambion. As described previously, siRNA oligonucleotides were transfected into subconfluent cells with Oligofectamine or Lipofectamine 2000 (Invitrogen) according to the manufacturer's instructions[6].

Cell culture. Cell culture including synchronization and transfection has been described previously[6,28]. Wild-type and *FBW7*$^{-/-}$ DLD1 cell lines were gifts from B. Vogelstein. Mouse T-ALL cell lines derived from *Tal1*-transgenic mice were gifts from M. A. Kelliher. Human T-ALL cell lines were previously described[2]. Loucy and CMLT1 T-ALL cell lines were obtained from J. Aster. For various assays described below, as indicated in the figure legends, T-ALL cells were cultured in either 0.5% FBS or 10% FBS-containing medium for sorafenib (ALEXIS Biochemicals) or ABT-737 (Symansis) treatment. In the case of combined treatment with both sorafenib and ABT-737, T-ALL cells were maintained in 10% FBS-containing medium. Lentiviral shRNA virus packaging, retrovirus packaging and subsequent infections were performed as described previously[28]. For cell viability assays, cells were plated at 10,000 per well in 96-well plates, and incubated with the appropriate medium containing sorafenib, ABT-737 or DMSO for 48 h. Assays were performed with CellTiter-Glo Luminescent Cell Viability Assay kit (Promega) according to the manufacturer's instructions. For detection of apoptosis, cells treated with various drugs were stained with propidium iodide (Roche) or co-stained with annexin-V–PE and 7-AAD (Annexin V-PE Apoptosis Detection Kit I, BD Bioscience) according to the manufacturer's instructions. Stained cells were sorted with a Dako-Cytomation MoFlo sorter (Dako) at the Dana-Farber Cancer Institute FACS core facility.

Immunoblotting and immunoprecipitation. Cells were lysed in EBC buffer (50 mM Tris, pH 8.0, 120 mM NaCl and 0.5% NP-40) supplemented with protease inhibitors (Complete Mini, Roche) and phosphatase inhibitors (phosphatase inhibitor cocktail set I and II, Calbiochem). The protein concentrations of the lysates were measured using the Bradford Protein Assay reagent (Bio-Rad) on a DU 800 spectrophotometer (Beckman Coulter). The lysates were then resolved by SDS–PAGE and immunoblotted with the indicated antibodies. For immunoprecipitation, 800 μg lysates were incubated with the appropriate antibody (1–2 μg) for 3–4 h at 4 °C followed by 1 h incubation with protein-A sepharose beads (GE Healthcare). Immuno-complexes were washed five times with NETN buffer (20 mM Tris, pH 8.0, 100 mM NaCl, 1 mM EDTA and 0.5% NP-40) before being resolved by SDS–PAGE and immunoblotted with the indicated antibodies. Quantification of the immunoblot band intensity was performed with ImageJ software.

Detection of MCL1 phosphorylation sites *in vivo*. To map MCL1 phosphorylation status *in vivo*, 293T cells were transfected with HA–MCL1 using the calcium phosphate method. Thirty hours after transfection, 293T cells were treated with 10 μM MG132 for 16 h to block the 26S proteasome pathway before collecting whole-cell lysates for HA–immunoprecipitation. After extensive washing with NETN buffer, the HA–immunoprecipitates were separated by SDS–PAGE and visualized with colloidal Coomassie blue. The band containing MCL1 was excised and treated with dithiothreitol (DTT) to reduce disulphide bonds and iodoacetamide to derivatize cysteine residues. In-gel digestion of the protein was done using trypsin or chymotrypsin. The resultant peptides were extracted from the gel and analysed by nanoscale-microcapillary reversed phase liquid chromatography tandem mass spectrometry (LC–MS/MS). Peptides were separated across a 37-min gradient ranging from 4% to 27% (v/v) acetonitrile in 0.1% (v/v) formic acid in a microcapillary (125 μm × 18 cm) column packed with C_{18} reversed-phase material (Magic C18AQ, 5 μm particles, 200 Å pore size, Michrom Bioresources) and online analysed on the LTQ Orbitrap XL hybrid FTMS (Thermo Scientific). For each cycle, one full MS scan acquired on the Orbitrap at high mass resolution was followed by ten MS/MS spectra on the linear ion trap XL from the ten most abundant ions. MS/MS spectra were searched using the SEQUEST algorithm against a database that was created based on a protein sequence database containing the sequence for MCL1. They were searched for common contaminants, such as human keratin protein with static modification of cysteine carboxymethylation, dynamic modification of methionine oxidation and serine, threonine and tyrosine phosphorylation. All peptide matches were filtered based on mass deviation, tryptic state, XCorr and dCn and confirmed by manual validation. The reliability of site localization of phosphorylation events was evaluated using the Ascore algorithm.

Real-time RT–PCR analysis. RNA was extracted using the RNeasy mini kit (Qiagen), and the reverse transcription (RT) reaction was performed using TaqMan Reverse Transcription Reagents (ABI, N808-0234). After mixing the resultant template with *MCL1* (Hs00172036_m1) or *GAPDH* (Hs99999905_m1) primers and TaqMan Fast Universal PCR Master Mix (ABI, 4352042), the real-time RT–PCR was performed with the 7500 Fast Real-time PCR system (ABI). *FBW7* (Hs00217794_m1), *SKP2* (Hs00180634_m1), *BTRC1* (Hs00182707_m1), *MCL1* (Hs00172036_m1) and *GAPDH* (Hs99999905_m1) primers were purchased from ABI.

Protein degradation analysis. Cells were transfected with Myc–MCL1 along with HA–FBW7 or Flag–β-TRCP1, and GFP as a negative control, in the presence or absence of HA–GSK3 and/or HA–ERK1. For half-life studies, cycloheximide (20 μg ml^{-1}; Sigma) was added to the media 40 h after transfection. At various time points thereafter, cells were lysed, and protein abundances were measured by immunoblotting analysis.

***In vivo* ubiquitylation assay.** Cells were transfected with a plasmid encoding Flag–Ub along with Myc–MCL1 and HA–FBW7 in the presence or absence of HA–GSK3. Thirty-six hours after transfection, cells were treated with the proteasome inhibitor MG132 (30 μM; Calbiochem) for 6 h and then collected. Anti-Myc immunoprecipitates were recovered and immunoblotted with anti-Flag antibody. Alternatively, cells were transfected with His–Ub along with Myc–MCL1 and HA–FBW7 in the presence or absence of HA–GSK3. Thirty-six hours after transfection,

cells were collected, and the lysates were incubated with Ni-NTA matrices (Qiagen) at 4 °C for 12 h in the presence of 8 M urea, pH 7.5. Immobilized proteins were washed five times with 8 M urea, pH 6.3, before being resolved by SDS–PAGE and immunoblotted with anti-Myc antibody.

***In vitro* ubiquitylation assay.** The *in vitro* ubiquitylation assays were performed as described previously[8]. To purify the SCF^{FBW7} E3 ligase complex, 293T cells were transfected with vectors encoding GST–FBW7, HA–CUL1, Myc–SKP1 and Flag–RBX1. The SCF^{FBW7} E3 complexes were purified from the whole-cell lysates using GST–agarose beads. Purified, recombinant GST–MCL1 proteins were incubated with purified SCF^{FBW7} complexes in the presence of purified, recombinant active E1, E2 (UBCH5A and UBCH3), ATP and ubiquitin. The reactions were stopped by the addition of 2× SDS–PAGE sample buffer, and the reaction products were resolved by SDS–PAGE gel and probed with the indicated antibodies.

***In vitro* kinase assay.** GSK3 was purchased from New England Biolabs. The *in vitro* kinase reaction was performed according to the manufacturer's instructions. Briefly, 5 μg indicated GST fusion proteins were incubated with purified active GSK3 in the presence of 5 μCi [γ-^{32}P]ATP and 200 μM cold ATP in the kinase reaction buffer for 20 min. The reaction was stopped by the addition of SDS-containing lysis buffer, the proteins resolved by SDS–PAGE and phosphorylation detected by autoradiography.

MCL1-binding assays. Binding to immobilized GST proteins was performed as described previously[28]. Where indicated, the GST–MCL1 proteins were incubated with GSK3 in the presence of ATP for 1 h before the binding assays.

Subcellular fractionation. Mitochondrial and cytosolic (S100) fractions were prepared by resuspending HeLa cells in 0.8 ml ice-cold buffer A (250 mM sucrose, 20 mM HEPES, pH 7.4, 10 mM KCl, 1.5 mM $MgCl_2$, 1 mM EDTA, 1 mM EGTA, 1 mM DTT, 17 μg ml^{-1} phenylmethylsulphonyl fluoride, 8 μg ml^{-1} aprotinin, 2 μg ml^{-1} leupeptin). Cells were then passed through an ice-cold cylinder cell homogenizer. Unlysed cells and nuclei were pelleted by a 10 min, 750 *g* spin. The recovered supernatant was spun at 10,000 *g* for 25 min. This pellet was resuspended in buffer A and represents the mitochondrial fraction. The supernatant was spun at 100,000 *g* for 1 h. The supernatant from this final centrifugation represents the S100 (cytosolic) fraction.

Mice. Generation of conditional *Fbw7* knockout mice (Lck-Cre/*Fbw7*$^{fl/fl}$ and Mx1-Cre/*Fbw7*$^{fl/fl}$) was described previously[3,4].

***In vivo* imaging.** CMLT1 cells were infected with lentiviral vectors encoding a shRNA directed against MCL1 (shMCL1) or an irrelevant control (shGFP). After selection in 1 μg ml^{-1} puromycin, cells were engineered for *in vivo* imaging by transduction with a retrovirus encoding a fusion of firefly luciferase fused to neomycin phosphotransferase and were then selected with 0.5 mg ml^{-1} G418. After selection, the luciferase activity of each engineered cell line was measured and found to have a similar reading. Subsequently, equal numbers of viable cells (0.5–1 × 10^7 cells) were injected into NOD SCID *Il2rg*-null mice through the lateral tail vein. Tumour burden was determined using bioluminescence imaging (IVIS Spectrum, Caliper Life Sciences) after intraperitoneal injection of 75 mg kg^{-1} D-luciferin. Total body luminescence was quantified using the Living Image software package (Caliper Life Sciences) and is expressed as photons per second per standardized region of interest (photons s^{-1} ROI^{-1}), encompassing the entire mouse. Data are presented as mean ± s.e.m. with statistical significance determined by Student's *t*-test.

27. Popov, N. *et al.* The ubiquitin-specific protease USP28 is required for MYC stability. *Nature Cell Biol.* **9,** 765–774 (2007).
28. Gao, D. *et al.* Phosphorylation by Akt1 promotes cytoplasmic localization of Skp2 and impairs APCCdh1-mediated Skp2 destruction. *Nature Cell Biol.* **11,** 397–408 (2009).
29. Benmaamar, R. & Pagano, M. Involvement of the SCF complex in the control of Cdh1 degradation in S-phase. *Cell Cycle* **4,** 1230–1232 (2005).
30. Chen, D. *et al.* ARF-BP1/Mule is a critical mediator of the ARF tumor suppressor. *Cell* **121,** 1071–1083 (2005).

nature medicine

UBE4B promotes Hdm2-mediated degradation of the tumor suppressor p53

Hong Wu[1], Scott L Pomeroy[2], Manuel Ferreira[3], Natalia Teider[2], Juliana Mariani[2], Keiichi I Nakayama[4], Shigetsugu Hatakeyama[5], Victor A Tron[6], Linda F Saltibus[7], Leo Spyracopoulos[7] & Roger P Leng[1]

The *TP53* gene (encoding the p53 tumor suppressor) is rarely mutated, although frequently inactivated, in medulloblastoma and ependymoma. Recent work in mouse models showed that the loss of p53 accelerated the development of medulloblastoma. The mechanism underlying p53 inactivation in human brain tumors is not completely understood. We show that ubiquitination factor E4B (UBE4B), an E3 and E4 ubiquitin ligase, physically interacts with p53 and Hdm2 (also known as Mdm2 in mice). UBE4B promotes p53 polyubiquitination and degradation and inhibits p53-dependent transactivation and apoptosis. Notably, silencing UBE4B expression impairs xenotransplanted tumor growth in a p53-dependent manner and overexpression of UBE4B correlates with decreased expression of p53 in these tumors. We also show that UBE4B overexpression is often associated with amplification of its gene in human brain tumors. Our data indicate that amplification and overexpression of *UBE4B* represent previously undescribed molecular mechanisms of inactivation of p53 in brain tumors.

The *TP53* tumor suppressor gene is inactivated in more than 50% of all human tumors, and *TP53* mutations are the most frequently observed genetic event in cancer cells. Thus, loss of p53 has a key role in cancer pathogenesis, and the regulation of p53 expression and its stability are essential for maintaining normal cell growth[1–6]. The ubiquitin ligase Mdm2 (mouse double minute 2) is a crucial negative regulator of p53 (refs. 7–11), and polyubiquitin chains are efficiently recognized by the proteasome[12–14]. Notably, Mdm2 mediates monoubiquitination or multiple-monoubiquitination of p53 (refs. 15–18). Mdm2 does not polyubiquitinate p53, which suggests that additional ubiquitin ligases or cofactors are required for Mdm2-mediated p53 polyubiquitination and degradation.

UBE4B is a human homolog of the *Saccharomyces cerevisiae* protein UFD2. Yeast UFD2 is involved in the ubiquitin fusion degradation (UFD) pathway and is encoded by a single-copy gene[19]. Yeast UFD2 is required for enzymatic activity in ubiquitin chain assembly and was the first E4 ubiquitination factor to be discovered[20]. Ubiquitin is an abundant and essential protein that mediates targeted protein degradation in eukaryotes. Ubiquitin-mediated protein degradation is a three-step process involving three enzymes: E1 (ubiquitin-activating enzyme), E2 (ubiquitin-conjugating enzyme), and E3 (ubiquitin protein ligase). A new class of ubiquitination enzyme, E4 (a ubiquitin chain assembly factor), was recently shown to be necessary for the degradation of some proteins via the ubiquitin fusion degradation (UFD) pathway[20]. Mouse Ube4b mediates ubiquitination in combination with E1 and E2, in the absence of other E3 components, by functioning as an E3 ligase *in vitro*[21]. Recently, it was reported that yeast UFD2 can also function as an E3 ubiquitin ligase[22]. E3 ligases often control the ubiquitination of multiple substrates[23]; for example, Ube4b serves as an E3 and/or E4 ligase for ataxin-3 (ref. 24), fasciculation and elongation protein ζ-1 (ref. 25) and the tumor suppressor p73 (ref. 26). Notably, deletion of mouse *Ube4b* results in marked apoptosis and lethality very early in embryonic development[27]; however, the underlying mechanisms for this lethality remain unclear.

In this study, we show that UBE4B physically interacts with p53 and Hdm2 and also negatively regulates the stability and function of p53. Our findings further show that UBE4B is overexpressed in various brain tumors, and that UBE4B expression and p53 status are inversely correlated in these tumors. Our data provide new insight into the mechanisms of p53 inactivation in brain tumors.

RESULTS

UBE4B physically interacts with Hdm2 and p53

We identified Ube4b as an Mdm2-interacting protein using the yeast two-hybrid system (data not shown). To determine whether endogenous UBE4B interacts with Hdm2 and p53 in human cells, we prepared extracts from human BJT fibroblast cells[28] and immunoprecipitated them with UBE4B-, Hdm2-, p53- or β-gal–specific antibodies (**Fig. 1a–d**). UBE4B coimmunoprecipitated with both Hdm2 and p53 (**Fig. 1a–c**). In a reciprocal experiment, Hdm2 and p53 also immunoprecipitated with UBE4B (**Fig. 1b–d**). An *in vitro* GST pull-down assay revealed that His-Ube4b bound GST-Mdm2 and

[1]Heritage Medical Research Center, Department of Laboratory Medicine and Pathology, University of Alberta, Edmonton, Alberta, Canada. [2]Department of Neurology, Children's Hospital Boston, Harvard Medical School, Boston, Massachusetts, USA. [3]Department of Neurosurgery, Massachusetts General Hospital, Harvard Medical School, Boston, Massachusetts, USA. [4]Department of Molecular and Cellular Biology, Medical Institute of Bioregulation, Kyushu University, Higashi-ku, Fukuoka, Japan. [5]Department of Molecular Biochemistry, Hokkaido University Graduate School of Medicine, Kita-ku, Sapporo, Japan. [6]Department of Pathology and Molecular Medicine, Queen's University, Kingston, Ontario, Canada. [7]Department of Biochemistry, University of Alberta, Edmonton, Alberta, Canada. Correspondence should be addressed to R.P.L. (rleng@ualberta.ca).

Received 8 April 2009; accepted 30 November 2010; published online 13 February 2011; doi:10.1038/nm.2283

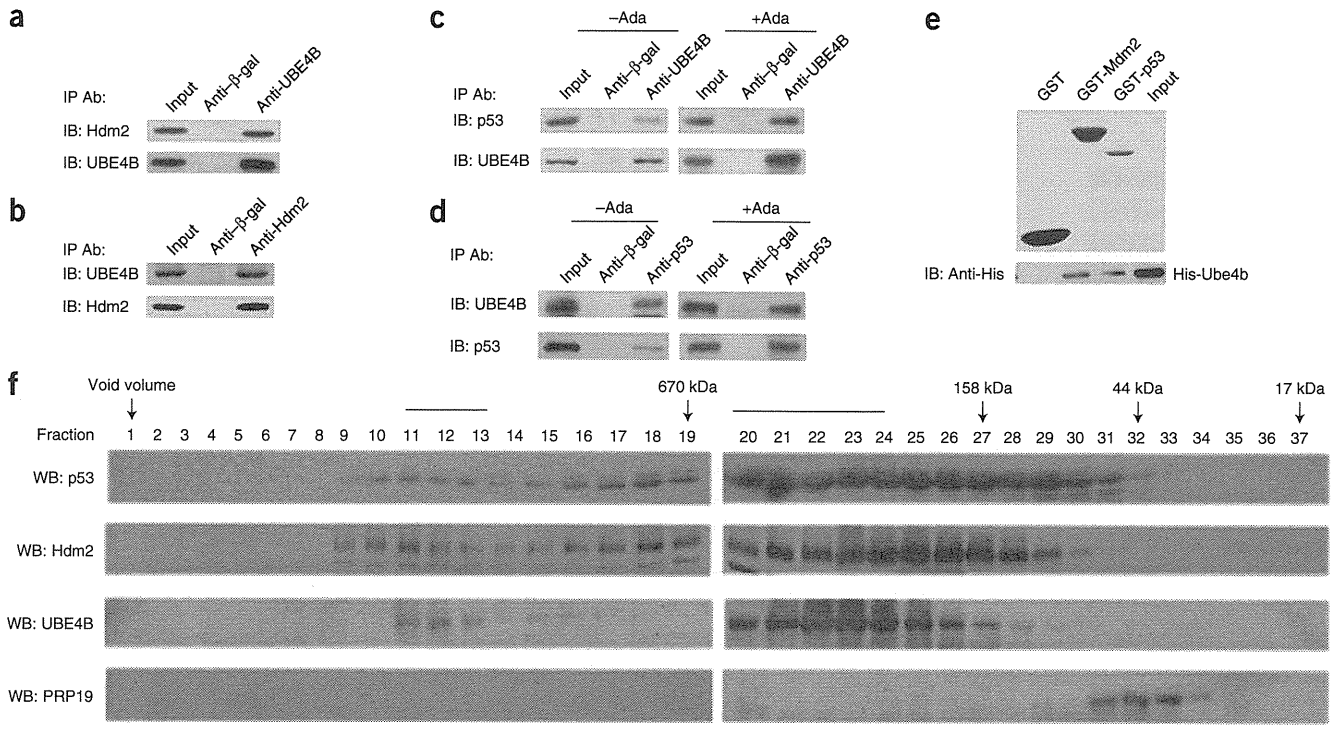

Figure 1 UBE4B interacts with Hdm2 and p53. (**a**) Western blot with UBE4B-specific or Hdm2-specific (2A10) antibodies after coimmunoprecipitation of Hdm2 from BJT whole cell lysates using UBE4B-specific (UFD2/E4) or β-gal–specific antibodies. (**b**) Western blot with UBE4B-specific and Hdm2-specific (2A10) antibodies after coimmunoprecipitation of UBE4B from BJT whole cell lysates using Hdm2-specific (2A10) or β-gal–specific antibodies. (**c**) Western blot of immunoprecipitates from BJT lysates with p53-specific (DO-1) and UBE4B-specific antibodies. BJT cells were treated with 10 μM of the proteasome inhibitor AdaAhx$_3$L$_3$VS (Ada) for 6 h or mock treated. Total lysates were immunoprecipitated with UBE4B-specific or β-gal–specific antibodies. (**d**) Western blot of BJT lysates with UBE4B-specific and p53-specific (DO-1) antibodies after BJT cells were treated with Ada for 6 h or mock treated. Total lysates were immunoprecipitated with p53-specific (DO-1) or β-gal–specific antibodies. (**e**) The *in vitro* interaction of Ube4b, Mdm2 and p53 was evaluated with GST pull-down assays and western blotting using an antibody against histidine (His-Ube4b). (**f**) BJT cell lysates were subjected to size-exclusion chromatography. Fractions were analyzed by western blotting for the presence of p53, Hdm2, UBE4B and PRP19 (control) with p53-specific (DO-1), Hdm2-specifc (2A10), UBE4B-specific (UFD2/E4) and PRP19-specific antibodies. The elution position of the molecular size markers is shown. In panels **a**–**e** are the eluted proteins probed by antibodies as shown. IB, immunoblot; IP, immunoprecipitation; WB, western blot.

GST-p53, but not GST alone (**Fig. 1e**). The Ube4b-interacting domains mapped to two regions of Mdm2 (amino acids 109–230 and 231–420) and to the amino acids of the DNA-binding domain and the C-terminal region in p53 (**Supplementary Fig. 1a–d**). We then investigated whether UBE4B, Hdm2 and p53 form a complex in cell extracts. BJT cell extracts were fractionated by gel filtration chromatography. We observed one major peak at 606–350 kDa (fractions 20–24), although the elution patterns of p53 and Hdm2 covered a wider range of fractions than that of UBE4B (**Fig. 1f**). In addition, we observed a smaller peak in fractions 11–13. These data indicate that p53, Hdm2 and UBE4B can form a ternary, or higher-order, complex in the cells. We next studied the kinetics of UBE4B or Ube4b induction in human or mouse isogenic pairs of cell lines[28] (**Supplementary Fig. 2a–d**) in response to p53 activation. The increase in UBE4B or Ube4b mRNA or protein was dependent on p53 (**Supplementary Fig. 2a–d**). We further found that the DNA sequences within intron 1 or intron 22 of *Ube4b* contain functional p53 DNA binding sites and are efficiently transactivated by wild-type p53 (**Supplementary Fig. 2e–g**).

Negative regulation of p53 by Ube4b

Transient overexpression of Ube4b reduced the amount of p53 protein, as did the coexpression of p53 and Mdm2 (**Fig. 2a**). We obtained similar results by overexpression of human UBE4B, Hdm2 and p53 (**Fig. 2b**). In parallel experiments, hemagglutinin (HA)-tagged ubiquitin (HA-Ub) was coexpressed in H1299 cells with plasmids encoding p53 or in combination with Ube4b, or Ube4bΔU (Ube4b in which the U-box has been deleted), or Mdm2, or Mdm2ΔRING, or Ube4b and Mdm2. p53 was immunoprecipitated and analyzed by western blotting with either an HA-specific antibody to detect ubiquitinated p53 (**Fig. 2c**) or a p53-specific antibody (Pab421) to detect total p53 (**Fig. 2c**). The p53 protein (or proteins associated with p53) appeared to be heavily ubiquitinated in the presence of Mdm2 and ubiquitinated to a lesser extent in the presence of Ube4b (**Fig. 2c**). To investigate whether Ube4b, a protein containing a U-box domain, specifically decreases the amount of p53 protein, we tested Ube4b and a number of other U-box–containing proteins for their ability to target p53 for degradation. We found that overexpression of Ube4b, but not of other U-box containing proteins, specifically reduced the amount of p53 protein that could be detected (**Fig. 2d**). To determine whether UBE4B mediates p53 degradation via the ubiquitin-proteasome pathway, we transfected human p53-null H1299 cells with plasmids expressing UBE4B and p53 and treated them with MG132, a proteasome inhibitor. The addition of MG132 greatly increased p53 abundance in the presence of transfected UBE4B compared with the untreated cells, suggesting that UBE4B promotes p53 degradation via the ubiquitin-proteasome pathway (**Fig. 2e**). Immunoprecipitation and western blotting revealed that the immunoprecipitated p53 was either monoubiquitinated or multiple monoubiquitinated in the presence of Hdm2 or polyubiquitinated in the presence of both Hdm2 and UBE4B when the cells were treated with MG132 (**Fig. 2f**).

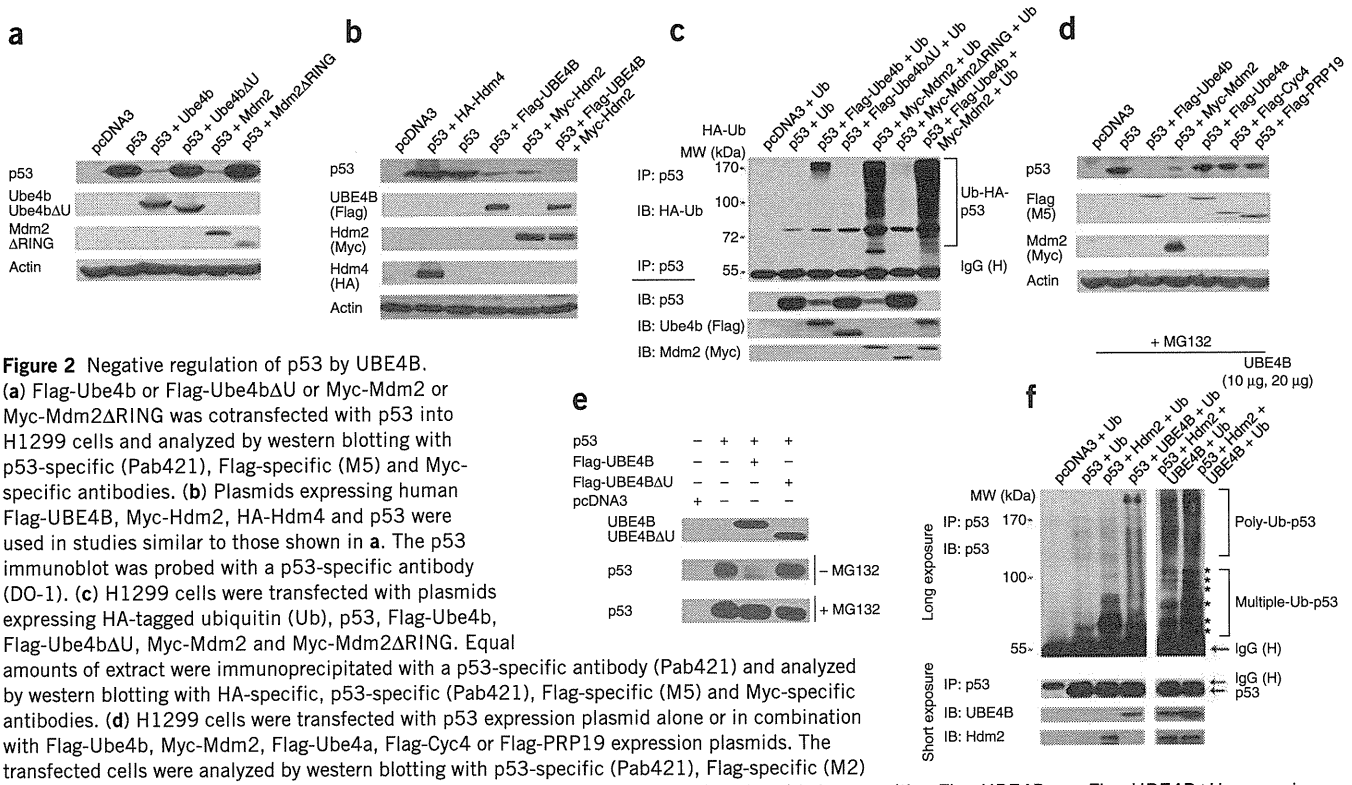

Figure 2 Negative regulation of p53 by UBE4B. (**a**) Flag-Ube4b or Flag-Ube4bΔU or Myc-Mdm2 or Myc-Mdm2ΔRING was cotransfected with p53 into H1299 cells and analyzed by western blotting with p53-specific (Pab421), Flag-specific (M5) and Myc-specific antibodies. (**b**) Plasmids expressing human Flag-UBE4B, Myc-Hdm2, HA-Hdm4 and p53 were used in studies similar to those shown in **a**. The p53 immunoblot was probed with a p53-specific antibody (DO-1). (**c**) H1299 cells were transfected with plasmids expressing HA-tagged ubiquitin (Ub), p53, Flag-Ube4b, Flag-Ube4bΔU, Myc-Mdm2 and Myc-Mdm2ΔRING. Equal amounts of extract were immunoprecipitated with a p53-specific antibody (Pab421) and analyzed by western blotting with HA-specific, p53-specific (Pab421), Flag-specific (M5) and Myc-specific antibodies. (**d**) H1299 cells were transfected with p53 expression plasmid alone or in combination with Flag-Ube4b, Myc-Mdm2, Flag-Ube4a, Flag-Cyc4 or Flag-PRP19 expression plasmids. The transfected cells were analyzed by western blotting with p53-specific (Pab421), Flag-specific (M2) and Myc-specific antibodies. (**e**) H1299 cells were transfected with a p53 expression plasmid alone or with a Flag-UBE4B or a Flag-UBE4BΔU expression plasmid in the presence or absence of MG132. The transfected cells were analyzed by western blotting with p53-specific (DO-1) or Flag-specific (M5) antibodies. (**f**) Extracts from cells treated with MG132 were immunoprecipitated with a p53-specific antibody (DO-1) and analyzed by western blotting with p53-specific (Ab-7), UBE4B-specific and Hdm2-specific (2A10) antibodies. Asterisks (*) indicate the migration positions of p53-ubiquitin (Ub-p53) conjugates. An antibody to β-actin (actin) was used as a loading control in panels **a–d**. IgG (H), IgG heavy chain.

Interdependence of UBE4B and Hdm2 in promoting p53 degradation

We tested the ability of UBE4B to regulate endogenous p53 protein in medulloblastoma wild-type p53-expressing H283 cells. The transient overexpression of UBE4B decreased the expression of p53 protein in these cells (**Fig. 3a**). To investigate whether endogenous Ube4b or UBE4B is crucial in regulating the expression level of p53 protein in mouse Neuro2A or human BJT cells, we examined six pairs of both UBE4B-targeting and Ube4b-targeting siRNAs. Two different siRNAs, Ube4b-siRNA1 and Ube4b-siRNA2, effectively knocked down the amount of Ube4b in mouse Neuro2A cells. The decrease in Ube4b was accompanied by an increase in p53 protein and its downstream targets, p21 and Mdm2 (**Fig. 3b**). Notably, a control scrambled siRNA had no effect on the amount of these proteins. We obtained similar results with human BJT cells (**Fig. 3c**).

To determine whether Ube4b promotes p53 degradation through Mdm2, we compared the ubiquitination-promoting activity of ectopically expressed Ube4b and Mdm2 in *Mdm2*$^{-/-}$ *Trp53*$^{-/-}$ mouse embryonic fibroblasts (MEFs). Notably, the overexpression of Ube4b slightly decreased p53 expression when p53 was coexpressed with Ube4b in Mdm2-null MEFs (**Fig. 3d**). In contrast, Ube4b expression greatly reduced the amount of p53 protein in the presence of transfected Mdm2 (**Fig. 3d**). The amount of p53 polyubiquitination was markedly decreased when p53 was coexpressed with Mdm2 in Ube4b-siRNA–treated Mdm2-null MEFs (**Fig. 3e**). We observed a stronger ubiquitinated signal in the presence of Mdm2, Ube4b, or Mdm2 and Ube4b together when the cells were treated with MG132 (**Fig. 3e**). Together, these results suggest that Mdm2 enhances Ube4b-dependent degradation of p53.

To investigate whether Ube4b is required for Mdm2-mediated p53 degradation *in vivo*, we transfected Neuro2A cells with Ube4b-siRNA2 or control siRNA. Two days later, we further transfected these cells with an Mdm2 expression plasmid. Overexpression of Mdm2 did not affect the amount of p53 protein when Ube4b was depleted, suggesting that Ube4b is required for Mdm2-promoted p53 degradation in these cells (**Fig. 3f**). As predicted, the basal level of endogenous p53 protein was also much higher in Ube4b-knockout (*Ube4b*$^{-/-}$) cells than in parental wild-type MEFs (**Fig. 3g**). Consistently, p53 expression was greatly decreased in the presence of transfected Ube4b, and to a lesser extent in either the presence of Ube4b and Ube4bΔU or in the presence of Ube4b alone when Mdm2 was eliminated in Ube4b-knockout MEFs (**Fig. 3h**). These findings suggest that Ube4bΔU may act as a dominant negative to interfere with Ube4b, and that Ube4b promotes p53 degradation that is dependent mainly on Mdm2. We also observed that depletion of Mdm2 did not increase p53 expression in Ube4b-knockout MEFs (**Fig. 3i**). p53 appeared to be heavily ubiquitinated in the presence of Mdm2 in wild-type MEFs, whereas most of these proteins appeared to be monoubiquitinated in Ube4b-knockout MEFs (**Fig. 3j**). However, we still detected >100-kDa p53-ubiquitin conjugates in Ube4b-knockout MEFs that overexpressed Mdm2, suggesting the existence of other molecules capable of targeting p53 for polyubiquitination (**Fig. 3j**). Furthermore, we detected the polyubiquitination of p53 in the presence of transfected Ube4b in Ube4b-knockout MEFs, but not in the presence of Ube4bΔU, suggesting that wild-type Ube4b can restore the function of Ube4b in Ube4b-knockout MEFs, but not Ube4bΔU (**Fig. 3j**). Pirh2 and Cop1 are RING-finger E3 ligases that are involved in the ubiquitination

and degradation of p53 (refs. 28–30). We observed that expression of Pirh2 with Ube4b or Cop1 with Ube4b enhanced the decrease in p53 expression when compared to Pirh2 or Cop1 overexpression alone (**Supplementary Fig. 3a,b**). These findings suggest that Ube4b may also cooperate with Pirh2 and Cop1 to downregulate p53.

The half-life of endogenous p53 in the presence of Ube4b was approximately 10 min ($P < 0.01$, **Supplementary Fig. 4b**), whereas it was approximately 20 min in cells transfected with an empty vector (**Supplementary Fig. 4a**). The half-life of endogenous p53 in the presence of the control siRNA was approximately 19 min; this half-life increased to approximately 32 min in cells depleted of Mdm2 (**Supplementary Fig. 4d**). Furthermore, the ablation of Ube4b increased the p53 half-life to approximately 35 min ($P < 0.05$); the half-life increased to approximately 61 min in cells depleted of both Ube4b and Mdm2 ($P < 0.05$, **Supplementary Fig. 4d**). We also examined the knockdown efficiency of Mdm2 and Ube4b (**Supplementary Fig. 4f**). Together, these data indicate that Ube4b, like Mdm2, regulates the stability of p53 *in vivo*.

UBE4B shows E4 activity *in vivo* and *in vitro*

To determine whether UBE4B functions as an E3/E4 ligase for p53 *in vivo*, we transfected H283 cells with siRNA constructs targeting specific sequences of UBE4B and, 40 h later, further transfected them with the HA-Ub expression plasmid and immunoprecipitated p53 with a p53-specific antibody (DO-1). Polyubiquitinated p53 abundance was markedly decreased by UBE4B-siRNA treatment when compared to treatment with the control siRNA (**Fig. 4a**). We saw increased polyubiquitination of p53 when the cells were treated with MG132 (**Fig. 4b**). We generated cell lines expressing shRNA against UBE4B (UBE4B-shA) or control-shA cell lines expressing HA-Ub

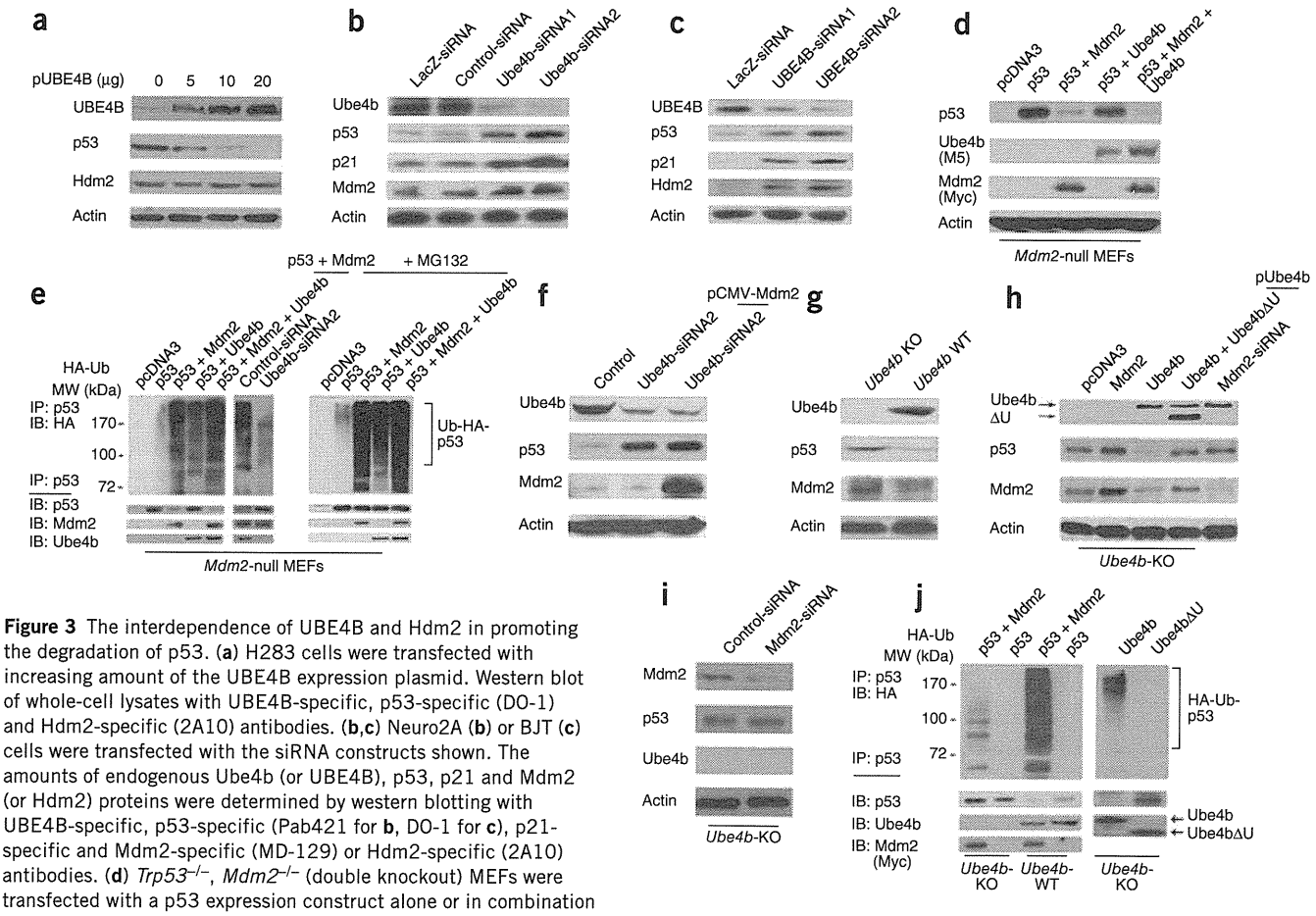

Figure 3 The interdependence of UBE4B and Hdm2 in promoting the degradation of p53. (**a**) H283 cells were transfected with increasing amount of the UBE4B expression plasmid. Western blot of whole-cell lysates with UBE4B-specific, p53-specific (DO-1) and Hdm2-specific (2A10) antibodies. (**b,c**) Neuro2A (**b**) or BJT (**c**) cells were transfected with the siRNA constructs shown. The amounts of endogenous Ube4b (or UBE4B), p53, p21 and Mdm2 (or Hdm2) proteins were determined by western blotting with UBE4B-specific, p53-specific (Pab421 for **b**, DO-1 for **c**), p21-specific and Mdm2-specific (MD-129) or Hdm2-specific (2A10) antibodies. (**d**) *Trp53*$^{-/-}$, *Mdm2*$^{-/-}$ (double knockout) MEFs were transfected with a p53 expression construct alone or in combination with a Myc-Mdm2 or Flag-Ube4b expression construct. The transfected cells were analyzed by western blot with p53-specific (Pab421), Flag-specific (for Ube4b) and Myc-specific (for Mdm2) antibodies. (**e**) Additionally, the extracts from the transfected cells were immunoprecipitated with a p53-specific antibody (Pab421) and analyzed by western blotting with HA-specific or p53-specific (Pab421) antibodies. MG132, a proteasome inhibitor, was added for 6 h before harvest as shown in the right panel. (**f**) Neuro2A cells were transfected with the Ube4b-siRNA2 construct or a control siRNA construct. Thirty hours later, the cells were further transfected with the Mdm2 expression plasmid and analyzed by western blot with Ube4b-specific (UFD2/E4), p53-specific (Pab421) and Mdm2-specific (MD-219) antibodies. (**g**) Cell extracts were prepared from *Ube4b*$^{-/-}$and *Ube4b*$^{+/+}$ MEFs. Western blot analysis of endogenous Ube4b, p53 and Mdm2 proteins with Ube4b-specific (UFD2/E4), p53-specific (CM5) and Mdm2-specific (MD-219) antibodies. (**h**) *Ube4b*$^{-/-}$ (Ube4b KO) MEFs were transfected with the indicated plasmids and analyzed by western blot with Flag-specific (for Ube4b and Ube4bΔU), Mdm2-specific (MD-219) and p53-specific (CM5) antibodies. (**i**) *Ube4b*$^{-/-}$ MEFs were transfected with control-siRNA or Mdm2-siRNA and analyzed by western blot with Mdm2-specific (MD-129), p53-specific (CM5) and Ube4b-specific antibodies. (**j**) *Ube4b*$^{-/-}$ MEFs or wild-type MEFs were cotransfected with plasmids expressing p53, or in combination with Myc-Mdm2, or Flag-Ube4b or Flag-Ube4bΔU as well as HA-Ub. Whole-cell lysates were immunoprecipitated with a p53-specific antibody (Pab421) and analyzed by western blot with HA-specific, p53-specific (Pab421), Flag-specific and Myc-specific antibodies. *Ube4b* KO, *Ube4b*$^{-/-}$ MEFs; *Ube4b* WT, *Ube4b*$^{+/+}$ MEFs. An antibody to β-actin (actin) was used as a loading control in all panels except **e** and **j**.

(**Fig. 4c**). The p53 immunoblot revealed that monoubiquitinated or multiple-monoubiquitinated p53 occurred to a lesser extent in control-shA than in UBE4B-shA cell lines, indicating an inverse correlation between the polyubiquinated and the monoubiquinated forms of p53 (**Fig. 4a–c**). These data show that UBE4B is required for p53 polyubiquitination *in vivo*.

To determine whether p53 could serve as a substrate for Ube4b-dependent ubiquitination *in vitro*, we performed *in vitro* ubiquitination assays[28]. We observed that Ube4b can function as an E3 ligase in promoting protein ubiquitination *in vitro* (**Fig. 4d**). Notably, the p53 immunoblot revealed that either Ube4b or Mdm2 alone promotes only the monoubiquitination of p53 *in vitro* (**Fig. 4d**). To directly test whether the smeared higher-molecular-weight species observed in **Figure 4d** represented polyubiquitinated forms of p53, we performed a coupled *in vitro* ubiquitination-immunoprecipitation. The p53 immunoblot shows that either Ube4b or Mdm2 mediated

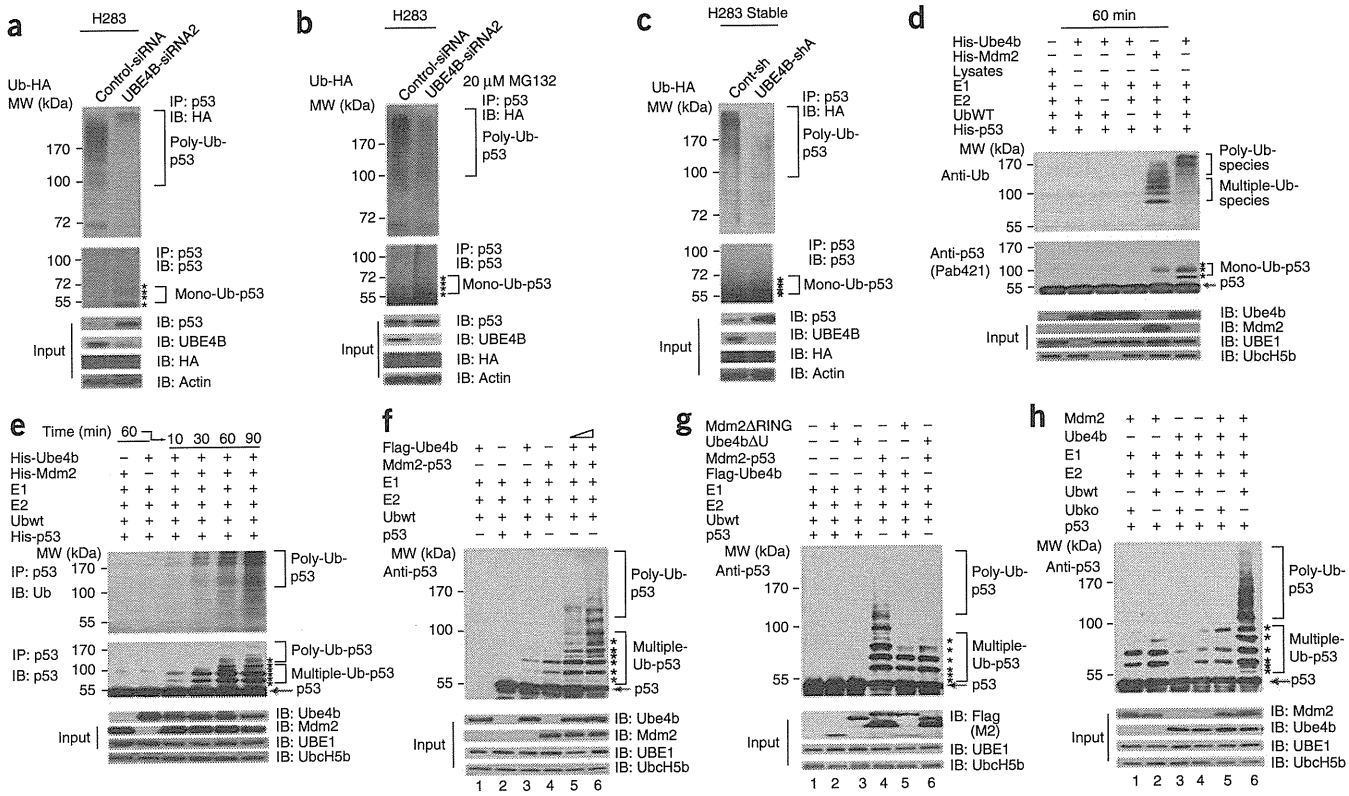

Figure 4 UBE4B mediates p53 polyubiquitination *in vivo* and *in vitro*. (**a**) H283 cells were transfected with control-siRNA or UBE4B-siRNA2. Forty hours later, cells were further transfected with the plasmid expressing HA-Ub. Lysates were immunoprecipitated with a p53-specific antibody (DO-1) and analyzed by immunoblotting with HA-specific, p53-specific (DO-1) and UBE4B-specific antibodies. (**b**) Similar to **a** except that after the second transfection of the HA-Ub expression plasmid, cells were treated with the proteasome inhibitor MG132 (20 μM) for 6 hours prior to harvest. (**c**) Stable depletion of UBE4B by siRNA in H283 cells. Similar to **a** except that the cell extracts were from the stably expressing UBE4B-siRNA2 or control-siRNA clones in H283 cells. (**d**) His-Ube4b was evaluated for E3 activity in the presence of recombinant E1, E2 (UbcH5b) and ubiquitin. Following the ubiquitination reaction, the samples were analyzed by western blotting with ubiquitin-specific and p53-specific (Pab421) antibodies. Direct western blots for Ube4b, Mdm2, UBE1 and UbcH5b are shown in the lower panel. (**e**) Western blot analysis of a coupled *in vitro* ubiquitination-immunoprecipitation. After the *in vitro* ubiquitination, the samples were immunoprecipitated with a p53-specific antibody (Pab421) and analyzed by western blotting with ubiquitin-specific and p53-specific antibodies. Direct western blots for Ube4b, Mdm2, UBE1 and UbcH5b are shown in the bottom blots. (**f**) Western blot of the *in vitro* ubiquitination reaction probed with a p53-specific (Pab421) antibody. Direct western blots for Ube4b, Mdm2, UBE1 and UbcH5b are shown in the lower panel. (**g**) Western blot similar to **f** except that the copurified Mdm2-p53 complexes were incubated with the purified Ube4bΔU, or the purified Ube4b was incubated with the purified Mdm2ΔRING. (**h**) Western blot of the *in vitro* ubiquitination reaction with a p53-specific antibody (Pab421). Direct western blots for Ube4b and Ube4bΔU (Ube4b polyclonal antibodies[21]), Mdm2 and Mdm2ΔRING (SMP14), UBE1 and UbcH5b are shown in the lower panel. (**i**) Purified HA-p53 was ubiquitinated by Flag-Hdm2 (ref. 31), then immunoprecipitated with HA antibody-conjugated beads to remove Hdm2 and nontagged ubiquitin. The immobilized p53 was then mixed in a second ubiquitination reaction, along with purified Flag-UBE4B and Flag-Ub. Western blot showing HA-p53-conjugates with a Flag-specific antibody (M2). In addition, we added Flag-Hdm2ΔRING as a negative control and Flag-CBP as a positive control. (**j**) U2OS cells were transfected plasmids expressing Flag-UBE4B or Flag-UBE4B 1001-1173. Cell lysates were immunoprecipitated with a p53-specific antibody (FL-393) and analyzed by western blotting with Hdm2-specific (2A10) and p53-specific (DO-1) antibodies. Direct western blot of the samples used is shown in the lower panel. Asterisks (*) indicate the migration positions of p53-ubiquitin conjugates. An antibody to β-actin (actin) was used as a loading control.

monoubiquitination of p53, whereas the combination of the two proteins promoted the polyubiquitination of p53 *in vitro* (**Fig. 4e**). We further confirmed this finding with baculovirus-expressed Mdm2 and Ube4b (**Fig. 4f–h**). The observation of longer chains suggests that Ube4b strongly stimulated the ubiquitination reaction (**Fig. 4f–h**). In addition, there was a dose-dependent increase in the abundance of the high-molecular-weight species of p53; this is consistent with polyubiquitination (**Fig. 4f**)[31]. Moreover, the reaction in the absence of p53 eliminated all p53 signal (**Fig. 4f**). Consistent with this, neither incubation of Mdm2ΔRING (Mdm2 without its RING domain) with Ube4b nor incubation of Ube4bΔU with Mdm2 promoted the polyubiquitination of p53 *in vitro* (**Fig. 4g**). We confirmed that Mdm2 catalyzes p53 monoubiquitination with wild-type ubiquitin or a lysineless ubiquitin mutant, Ubko, that cannot form polyubiquitin chains (**Fig. 4h**). We also found that Mdm2ΔRING or Ube4bΔU partially inhibits Mdm2-mediated or Ube4b-mediated p53 ubiquitination, respectively (**Supplementary Fig. 3c**). Together, these data show that Ube4b functions as an E4 ligase together with Mdm2 to promote p53 polyubiquitination *in vitro*.

To further determine the independent contribution of UBE4B to p53 polyubiquitination, we performed a two-step, *in vitro* E4 assay[31]. We found that UBE4B functions as an E4 ligase for p53 and is dependent mainly on Hdm2 (**Fig. 4i**). However, the E4 ligase function of UBE4B was not absolutely dependent on Hdm2, because we detected a weak signal of poly–Ub-p53 (**Fig. 4i**). Next, we analyzed the effect of UBE4B overexpression on the interaction of Hdm2 and p53. Overexpression of UBE4B reduced the amount of p53, but this did not occur with cells overexpressing UBE4B 1001–1173 (Hdm2 binding-defective mutant) (**Fig. 4j**). Notably, the interaction of Hdm2 and p53 was not substantially changed in the presence of UBE4B. Together, these data indicate that, unlike YY1 (Yin-Yang protein 1)[32], UBE4B is not likely to be required as a molecular clamp for the interaction of Hdm2 and p53.

UBE4B inhibits p53-dependent transactivation and apoptosis

To investigate the functional consequences of the interaction of UBE4B with p53, we examined the effect of UBE4B expression on p53-mediated transcriptional activation. We found that UBE4B and Hdm2 both repressed p53-dependent transactivation (**Fig. 5a**). Moreover, the UBE4BΔU mutant retained the ability to repress p53-dependent transactivation, suggesting that UBE4B impairs the transactivation function of p53 without targeting it for degradation (**Fig. 5a**). We observed that UBE4B, like Hdm2, can inhibit p53-dependent cell death by long-term colony assays (**Supplementary Fig. 5a,b**). Additionally, we used annexin V staining to determine whether transient UBE4B expression could rescue cells from p53-dependent cell death. The expression of p53 alone resulted in increased apoptosis (**Fig. 5b**). However, the increase in apoptosis could be largely prevented by the coexpression of UBE4B or Hdm2 (**Fig. 5b**). We also discovered that the overexpression of Hdm2 did not rescue cells from p53-mediated cell death when UBE4B was depleted (**Fig. 5c**). The cell cycle arrest that is mediated by p53 is crucial for its tumor suppression function, so we determined whether the inhibition of UBE4B enabled p53 to arrest cells in the G1 phase of the cell cycle. We transfected human BJT fibroblast cells or BJT/DD fibroblast cells (an isogenic derivative expressing the C-terminal fragment of p53 as a dominant-negative p53) with LacZ-siRNA (used as a negative control) or UBE4B-siRNA2. We also examined the knockdown efficiency of UBE4B (**Fig. 5d**). The siRNA-mediated disruption of UBE4B potentiated the ability of p53 to arrest BJT fibroblasts in the G1 phase of the cell cycle (**Fig. 5e**), but this did not occur in the isogenic derivative, BJ/DD (**Fig. 5f**; ref. 28). Together, these data show that UBE4B is involved in the regulation of p53-dependent transactivation and apoptosis as well as in p53-mediated checkpoint control.

Ube4b promotes tumorigenesis and is elevated in brain tumors

Next, we examined the ability of Ube4b to immortalize primary rat embryonic fibroblasts (REFs). Similar to a previously reported technique for Mdm2 (ref. 33), either Ube4b or Ube4b and an *Hras* (Harvey rat sarcoma virus oncogene) gene were used to generate immortal cell lines (**Supplementary Table 1** and **Supplementary Methods**). We then analyzed the transforming ability of Ube4b by evaluating the cells' capacity for anchorage-independent growth in REFs. The ectopic expression of Ube4b alone did not induce growth in soft agar (**Supplementary Fig. 6a**). However, Ube4b dramatically increased the transformation activity of oncogenic *Hras* in soft-agar colony formation assays (**Supplementary Fig. 6a**), which indicates that Ube4b can cooperate with an activated *Hras* gene to transform primary cells. We found that focus formation was suppressed by p53 in MEFs, which we used because *Trp53*$^{-/-}$ MEFs are often used for p53 focus formation experiments; *Trp53*$^{-/-}$ MEFs produced more foci than wild-type MEFs[34,35]. Similar soft agar assays revealed that overexpression of Ube4b in a p53-null background failed to increase the transformation activity of *Hras* (**Supplementary Fig. 6b**). Together, these data indicate that the oncogenic activity of Ube4b is mainly p53 dependent (**Supplementary Fig. 6c**). The combined effects of Ube4b and *Hras* on the transformation of REFs are summarized in **Supplementary Table 1**.

To examine the role of Ube4b in tumor formation *in vivo*, we injected NIH3T3 mouse fibroblast cells expressing an empty vector or vector encoding Ube4bΔU or Ube4b into severe combined immunodeficiency (SCID) mice. SCID mice injected with NIH3T3 cells expressing Ube4b developed large tumors in 3 weeks (n = 10) (**Fig. 6a**). In contrast, NIH3T3 cells expressing Ube4bΔU or an empty vector did not generate any tumors. Given that Ube4b has oncogenic potential, we further examined whether the elimination of Ube4b expression by siRNA could inhibit tumor growth. We used two colorectal cancer cell lines: wild-type human HCT116 (HCT116-WT) and HCT116 *TP53*$^{-/-}$ (refs. 36,37). SCID mice injected with HCT116-WT cells expressing LacZ-siRNA developed large tumors, whereas mice injected with HCT116-WT cells expressing UBE4B-siRNA developed considerably smaller tumors (n = 10) (**Fig. 6b**). In contrast, HCT116 *TP53*$^{-/-}$ cells that express UBE4B-siRNA only showed a slight effect on tumor growth compared with cells that express LacZ-siRNA (**Fig. 6b**). We then studied the kinetics of tumor appearance and development in these mice. We found that high Ube4b expression was accompanied by low p53 expression in the Ube4b-expressing tumors (**Fig. 6c**), which suggests that Ube4b induces tumorigenesis by inactivating p53 *in vivo*. As expected, the depletion of UBE4B by siRNA had no effect on p21 protein in HCT116 *TP53*$^{-/-}$ cells (**Fig. 6d**). In contrast, the decrease in UBE4B expression was accompanied by increased levels of p53 and its downstream target, p21, in HCT116-WT (**Fig. 6e**) but not HCT116 *TP53*$^{-/-}$ cells (**Fig. 6d**). Together, these data indicate that the overexpression of UBE4B promotes tumor growth and that the elimination of UBE4B is effective in inhibiting growth of p53-expressing tumors.

We next examined whether Ube4b expression is related to the status of p53 in various brain tumors. We found that Ube4b was overexpressed in medulloblastoma tissues derived from *Ptch*$^{+/-}$ (encoding patched homolog-1) mice (**Fig. 6f**), and UBE4B was overexpressed in human medulloblastoma cell lines (**Fig. 6g**), in human medulloblastoma tissues (**Fig. 6h**), in human ependymoma tissues (**Fig. 6i**) and in human pediatric astrocytoma tissues (**Fig. 6j**). We identified